



Angular analysis of $B^0 \rightarrow D^{*-} D_s^{*+}$ with $D_s^{*+} \rightarrow D_s^+ \gamma$ decays

LHCb collaboration[†]

Abstract

The first full angular analysis of the $B^0 \rightarrow D^{*-} D_s^{*+}$ decay is performed using 6 fb^{-1} of pp collision data collected with the LHCb experiment at a centre-of-mass energy of 13 TeV. The $D_s^{*+} \rightarrow D_s^+ \gamma$ and $D^{*-} \rightarrow \bar{D}^0 \pi^-$ vector meson decays are used with the subsequent $D_s^+ \rightarrow K^+ K^- \pi^+$ and $\bar{D}^0 \rightarrow K^+ \pi^-$ decays. All helicity amplitudes and phases are measured, and the longitudinal polarisation fraction is determined to be $f_L = 0.578 \pm 0.010 \pm 0.011$ with world-best precision, where the first uncertainty is statistical and the second is systematic. The pattern of helicity amplitude magnitudes is found to align with expectations from quark-helicity conservation in B decays. The ratio of branching fractions $[\mathcal{B}(B^0 \rightarrow D^{*-} D_s^{*+}) \times \mathcal{B}(D_s^{*+} \rightarrow D_s^+ \gamma)] / \mathcal{B}(B^0 \rightarrow D^{*-} D_s^+)$ is measured to be $2.045 \pm 0.022 \pm 0.071$ with world-best precision. In addition, the first observation of the Cabibbo-suppressed $B_s^0 \rightarrow D^{*-} D_s^+$ decay is made with a significance of seven standard deviations. The branching fraction ratio $\mathcal{B}(B_s^0 \rightarrow D^{*-} D_s^+) / \mathcal{B}(B^0 \rightarrow D^{*-} D_s^+)$ is measured to be $0.049 \pm 0.006 \pm 0.003 \pm 0.002$, where the third uncertainty is due to limited knowledge of the ratio of fragmentation fractions.

Published in JHEP 06 (2021) 177.

© 2021 CERN for the benefit of the LHCb collaboration. CC BY 4.0 licence.

[†]Authors are listed at the end of this paper.

1 Introduction

The $B^0 \rightarrow D^{*-} D_s^{*+}$ decay involves the production of two vector charm mesons from a pseudoscalar B^0 parent. This process exhibits a polarisation structure, where three complex helicity amplitudes H_0 , H_+ , and H_- contribute to the total decay rate. These amplitudes correspond to the relative orientation of the linear polarisation vectors of the two vector mesons. Parity-even (\parallel) and parity-odd (\perp) transversity amplitudes can also be defined in terms of H_+ and H_- , namely $A_{\parallel,\perp} = (H_+ \pm H_-)/\sqrt{2}$. The helicity amplitudes can interfere, with interference governed by the strong phases of the transverse components, ϕ_+ and ϕ_- , relative to the phase of the longitudinal component, ϕ_0 , which is conventionally taken to be equal to zero. Therefore, five parameters in total determine the decay rate:

- $|H_0|$, the magnitude of the longitudinal amplitude;
- $|H_+|$ and $|H_-|$, the magnitudes of the two transverse amplitudes;
- ϕ_+ and ϕ_- , the phases of the transverse amplitudes relative to H_0 .

In order to normalise the total decay rate, $|H_0|^2 + |H_+|^2 + |H_-|^2 = f_L + f_T = 1$ is required, where $f_L \equiv |H_0|^2$ is the longitudinal polarisation fraction and $f_T \equiv |H_+|^2 + |H_-|^2$ is the transverse polarisation fraction. The current world average for f_L is 0.52 ± 0.05 [1, 2], while theoretical predictions cover a similar range [3–6]; the transverse helicity amplitudes have not been measured previously. The normalisation condition reduces the total number of independent observables to four, where the additional observable is absorbed into the absolute branching fraction of the decay which is not measured. Measuring the relative magnitudes of the helicity amplitudes offers a test of quark-helicity conservation in this tree-level decay involving a $b \rightarrow c$ quark transition. In such decays, a $|H_0| > |H_+| > |H_-|$ hierarchy is expected [7], where the $V - A$ nature of the weak interaction causes the longitudinal component to dominate.

The $B^0 \rightarrow D^{*-} D_s^{*+}$ decay has a large branching fraction, $\mathcal{B}(B^0 \rightarrow D^{*-} D_s^{*+}) = (1.77 \pm 0.14)\%$ [2], and is thus a prominent background in $B^0 \rightarrow D^{*-} \tau^+ \nu_\tau$ analyses that exploit the hadronic three-prong $\tau^+ \rightarrow \pi^+ \pi^+ \pi^- \bar{\nu}_\tau$ mode in order to measure the ratio $R(D^*) \equiv \mathcal{B}(B^0 \rightarrow D^{*-} \tau^+ \nu_\tau) / \mathcal{B}(B^0 \rightarrow D^{*-} \ell^+ \nu_\ell)$ [8] or the angular coefficients of the $B^0 \rightarrow D^{*-} \tau^+ \nu_\tau$ decay [9]. Such a background arises when the neutral particle produced in the D_s^{*+} decay is not reconstructed, and the D_s^+ meson decays to three pions plus additional non-reconstructed particles.

Using data corresponding to an integrated luminosity of 6 fb^{-1} collected at a centre-of-mass energy of 13 TeV with the LHCb experiment between 2015 and 2018, $B^0 \rightarrow D^{*-} D_s^{*+}$ with $D_s^{*+} \rightarrow D_s^+ \gamma$ decays are reconstructed via the $D^{*-} \rightarrow (\bar{D}^0 \rightarrow K^+ \pi^-) \pi^-$ and $D_s^+ \rightarrow K^+ K^- \pi^+$ channels; the inclusion of charge-conjugate processes is implied throughout. Partially reconstructed decays, where the photon is not considered in the invariant-mass calculation, are used in a fit to the $m(D^{*-} D_s^+)$ distribution to measure f_L . Fully reconstructed decays are then considered in a subsequent angular analysis to measure the remaining helicity observables. Measurements are performed under the assumption that both the $\bar{D}^0 \pi^-$ and $D_s^+ \gamma$ systems are pure vector, as no evidence for a scalar contribution is found in the $m(\bar{D}^0 \pi^-)$ distribution in data and no scalar component is permitted in $m(D_s^+ \gamma)$ due to the photon angular momentum. The analysis includes an improved

measurement of f_L and first measurements of the transverse helicity amplitude magnitudes and phases.

The data sample is also used to measure the ratio of branching fractions $\mathcal{R} \equiv [\mathcal{B}(B^0 \rightarrow D^{*-}D_s^{*+}) \times \mathcal{B}(D_s^{*+} \rightarrow D_s^+\gamma)]/\mathcal{B}(B^0 \rightarrow D^{*-}D_s^+)$, where the current value of $\mathcal{R} = 2.07 \pm 0.33$ is calculated using world-average branching fractions taken from Ref. [2]. In addition, a measurement of the previously unobserved Cabibbo-suppressed $B_s^0 \rightarrow D^{*-}D_s^+$ decay is performed and the ratio of branching fractions $\mathcal{B}(B_s^0 \rightarrow D^{*-}D_s^+)/\mathcal{B}(B^0 \rightarrow D^{*-}D_s^+)$ determined.

The formalism adopted is described in Sect. 2, essential details of the LHCb detector and simulation are given in Sect. 3, and the event selection is outlined in Sect. 4. The longitudinal polarisation fraction and ratios of branching fractions are measured in Sect. 5, and the remaining helicity observables are measured in Sects. 6–8. Systematic uncertainties are determined in Sect. 9, and final results and conclusions are presented in Sect. 10.

2 Angular decay rate formalism

The $B^0 \rightarrow D^{*-}D_s^{*+}$ decay rate is a function of three decay angles, θ_D , θ_X , and χ , where θ_D is the angle between the \bar{D}^0 meson and the direction opposite the B^0 momentum vector in the D^{*-} rest frame, θ_X is the angle between the D_s^{*+} meson and the direction opposite the B^0 momentum vector in the D_s^{*+} rest frame, and χ is the angle between the two decay planes as defined in the B^0 rest frame. The angles are illustrated in Fig. 1, and are explicitly defined as follows

$$\begin{aligned}
\cos \theta_D &= \left(\hat{p}_{D^0}^{(D^{*-})} \right) \cdot \left(\hat{p}_{D^{*-}}^{(B^0)} \right) = \left(\hat{p}_{D^0}^{(D^{*-})} \right) \cdot \left(-\hat{p}_{B^0}^{(D^{*-})} \right), \\
\cos \theta_X &= \left(\hat{p}_{D_s^+}^{(D_s^{*+})} \right) \cdot \left(\hat{p}_{D_s^{*+}}^{(B^0)} \right) = \left(\hat{p}_{D_s^+}^{(D_s^{*+})} \right) \cdot \left(-\hat{p}_{B^0}^{(D_s^{*+})} \right), \\
\cos \chi &= \left(\hat{p}_{D_s^+}^{(B^0)} \times \hat{p}_\gamma^{(B^0)} \right) \cdot \left(\hat{p}_{D^0}^{(B^0)} \times \hat{p}_{\pi^-}^{(B^0)} \right), \\
\sin \chi^{B^0} &= - \left[\left(\hat{p}_{D_s^+}^{(B^0)} \times \hat{p}_\gamma^{(B^0)} \right) \times \left(\hat{p}_{D^0}^{(B^0)} \times \hat{p}_{\pi^-}^{(B^0)} \right) \right] \cdot \hat{p}_{D^{*-}}^{(B^0)}, \\
\sin \chi^{\bar{B}^0} &= + \left[\left(\hat{p}_{D_s^-}^{(\bar{B}^0)} \times \hat{p}_\gamma^{(\bar{B}^0)} \right) \times \left(\hat{p}_{D^0}^{(\bar{B}^0)} \times \hat{p}_{\pi^-}^{(\bar{B}^0)} \right) \right] \cdot \hat{p}_{D^{*+}}^{(\bar{B}^0)},
\end{aligned} \tag{1}$$

where the $\hat{p}_X^{(Y)}$ are unit vectors describing the direction of a particle X in the rest frame of the system Y . In the B^0 rest frame, the angular definition for the \bar{B}^0 decay is a charge-parity (CP) transformation of that for the B^0 decay. The sign of $\sin \chi$ is negative for B^0 candidates and positive for \bar{B}^0 candidates, where the B -meson flavour is tagged by the D^* -meson charge. This formalism is the same as that adopted in other LHCb angular analyses such as that of $B \rightarrow K^*\mu^+\mu^-$ decays [10, 11].

The full three-dimensional differential decay rate expressed in terms of the helicity

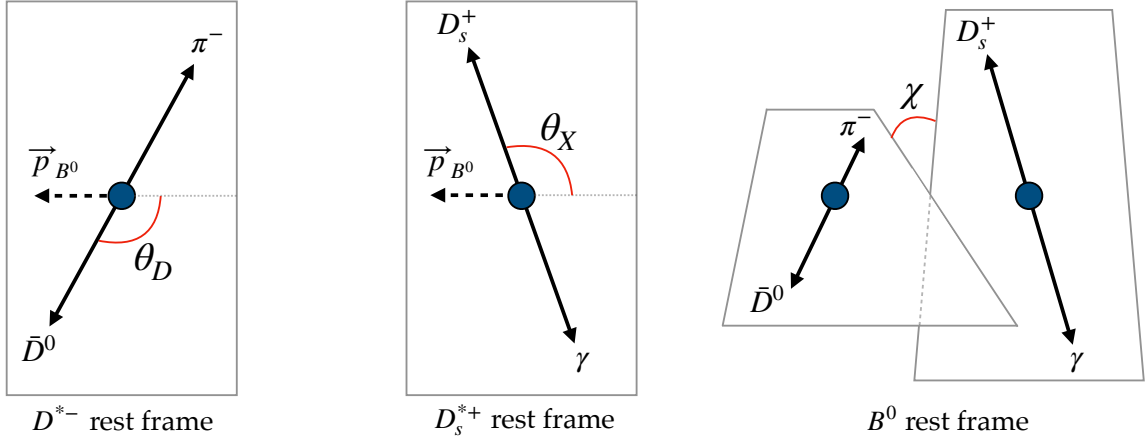


Figure 1: Illustration of the $B^0 \rightarrow D^{*-} D_s^{*+}$ decay angles.

amplitudes is given by [3]

$$\begin{aligned}
 \frac{d^3\Gamma}{d\cos\theta_D d\cos\theta_X d\chi} &\propto \frac{9}{8} \left\{ \cos^2\theta_D \sin^2\theta_X |H_0|^2 + \frac{1}{4} \sin^2\theta_D (1 + \cos^2\theta_X) (|H_+|^2 + |H_-|^2) \right. \\
 &- \frac{1}{2} \sin^2\theta_D \sin^2\theta_X [\cos 2\chi \operatorname{Re}(H_+ H_-^*) - \sin 2\chi \operatorname{Im}(H_+ H_-^*)] \\
 &\left. - \frac{1}{4} \sin 2\theta_D \sin 2\theta_X [\cos \chi \operatorname{Re}(H_+ H_0^* + H_- H_0^*) - \sin \chi \operatorname{Im}(H_+ H_0^* - H_- H_0^*)] \right\}.
 \end{aligned} \tag{2}$$

3 LHCb detector and simulation

The LHCb detector [12, 13] is a single-arm forward spectrometer covering the pseudorapidity range $2 < \eta < 5$, designed for the study of particles containing b - or c -quarks. The detector includes a high-precision tracking system consisting of a silicon-strip vertex detector surrounding the pp interaction region, a large-area silicon-strip detector located upstream of a dipole magnet with a bending power of about 4 Tm, and three stations of silicon-strip detectors and straw drift tubes placed downstream of the magnet. The tracking system provides a measurement of the momentum, p , of charged particles with a relative uncertainty that varies from 0.5% at low momentum to 1.0% at 200 GeV/ c . The minimum distance of a track to a primary pp collision vertex (PV), the impact parameter (IP), is measured with a resolution of $(15 + 29/p_T) \mu\text{m}$, where p_T is the component of the momentum transverse to the beam, in GeV/ c . Different types of charged hadrons are distinguished using information from two ring-imaging Cherenkov

detectors. Photons, electrons and hadrons are identified by a calorimeter system consisting of scintillating-pad and preshower detectors, an electromagnetic and a hadronic calorimeter. Muons are identified by a system composed of alternating layers of iron and multiwire proportional chambers.

The online event selection is performed by a trigger, which consists of a hardware stage, based on information from the calorimeter and muon systems, followed by a software stage, which applies a full event reconstruction. At the hardware trigger stage, events are required to have a muon with high p_T or a hadron, photon or electron with high transverse energy in the calorimeters. For hadrons, the transverse energy threshold is 3.5 GeV. The software trigger requires a two-, three- or four-track secondary vertex with a significant displacement from any primary pp interaction vertex. At least one charged particle must have a transverse momentum $p_T > 1.6 \text{ GeV}/c$ and be inconsistent with originating from any PV. A multivariate algorithm is used for the identification of secondary vertices consistent with the decay of a b hadron. In the offline selection, trigger information is associated with reconstructed particles. Selection requirements can therefore be made on the trigger selection itself and on whether the decision was due to the signal candidate, other particles produced in the pp collision, or an overlap of both.

Simulation is required to model the effects of the detector acceptance and the imposed selection requirements. In the simulation, pp collisions are generated using PYTHIA [14] with a specific LHCb configuration [15]. Decays of unstable particles are described by EVTGEN [16], in which final-state radiation is generated using PHOTOS [17]. The interaction of the generated particles with the detector, and its response, are implemented using the GEANT4 toolkit [18] as described in Ref. [19]. The underlying pp interaction is reused multiple times, with an independently generated signal decay for each [20]. In addition, the $m(D^{*-}D_s^+)$ distributions of pure longitudinal and transverse polarised $B^0 \rightarrow D^{*-}D_s^{*+}$ decays are studied using fast-simulated samples generated with the RAPIDSIM package [21], where an LHCb momentum resolution configuration is used to smear the generated four-momenta. The same tool is used to study the $m(D^{*-}D_s^+)$ distributions of various background contributions from decays involving higher-excited charm mesons.

4 Event selection

Candidate $B^0 \rightarrow D^{*-}D_s^+$ decays are reconstructed through the $D^{*-} \rightarrow (\bar{D}^0 \rightarrow K^+\pi^-)\pi^-$ and $D_s^+ \rightarrow K^+K^-\pi^+$ channels. The tracks of the final-state particles are required to have a good quality, fulfil loose particle identification (PID) criteria, and have a high χ_{IP}^2 value with respect to any PV, where χ_{IP}^2 is defined as the difference in the vertex-fit χ^2 of a given PV reconstructed with and without the particle being considered. The reconstructed masses of the \bar{D}^0 and D_s^+ candidates are required to lie inside mass windows of $\pm 20 \text{ MeV}/c^2$ around their known values [2]. The D^{*-} candidate mass is required to be within $\pm 40 \text{ MeV}/c^2$ of the known value [2], while the difference in mass between the D^{*-} and \bar{D}^0 candidates is required to be in the range 140–150 MeV/c^2 . In combination with the track PID cuts, these narrow mass windows reduce potential backgrounds from misidentified decays such as $B^0 \rightarrow D^{*-}D^+$ to negligible levels.

The B^0 candidate is reconstructed by combining the D^{*-} and D_s^+ candidates to form a common vertex. If multiple PVs are reconstructed in the same event, the PV for which the B^0 candidate has the lowest χ_{IP}^2 is assigned as the associated PV. The

p_T of the B^0 candidate is required to be larger than $5 \text{ GeV}/c$, and the χ_{IP}^2 of the B^0 candidate for the associated PV is required to be small. To suppress combinatorial background and background from decays involving the production of a D^{*-} and three prompt tracks, the flight distance of the D_s^+ candidate along the beam axis is required to be different from zero by more than one standard deviation, considering both the origin and decay-vertex uncertainties of the D_s^+ candidate. To suppress combinatorial background from combinations of tracks originating from the PV, the decay time of the B^0 candidate is required to be larger than 0.2 ps . To improve the invariant-mass resolution, a kinematic fit is performed to the decay chain [22], the B^0 candidate is constrained to originate from the PV and the D_s^+ and \bar{D}^0 masses are constrained to their known values. Candidates are retained if the resulting invariant mass of the $D^{*-}D_s^+$ combination falls within the $4900\text{--}5500 \text{ MeV}/c^2$ range, which includes the region occupied by partially reconstructed $B^0 \rightarrow D^{*-}D_s^{*+}$ decays when the neutral particle produced in the D_s^{*+} decay is not reconstructed. This sample is considered in Sect. 5, where a fit to the $m(D^{*-}D_s^+)$ distribution of candidates is used to measure f_L .

A subsample of fully reconstructed $B^0 \rightarrow D^{*-}D_s^{*+}$ candidates is selected by combining D_s^+ candidates from the above dataset with photons. The difference between the D_s^{*+} and D_s^+ candidate masses is required to be in the range $120\text{--}180 \text{ MeV}/c^2$, and the photon is required to have a p_T larger than $500 \text{ MeV}/c$. Each D_s^{*+} candidate is then recombined with the corresponding D^{*-} candidate from the above dataset to form a B^0 candidate, where candidates in the invariant-mass range $5150\text{--}5500 \text{ MeV}/c^2$ are retained. Fully reconstructed candidates with $m(D^{*-}D_s^+)$ values greater than $5240 \text{ MeV}/c^2$ are vetoed to remove $B^0 \rightarrow D^{*-}D_s^+$ decays where a random photon is combined with the D_s^+ candidate. This dataset is used in Sect. 8 to measure the remaining helicity observables in an angular analysis.

5 Measurement of f_L and branching fraction ratios

The longitudinal polarisation fraction, f_L , determines the fractional contribution of the H_0 helicity amplitude to the total $B^0 \rightarrow D^{*-}D_s^{*+}$ decay rate. The longitudinal and transverse amplitudes contribute to the one-dimensional differential decay rate in $\cos \theta_X$ as follows,

$$\begin{aligned} \frac{d\Gamma}{d\cos\theta_X} &\propto \frac{3}{4} \left[|H_0|^2(1 - \cos^2\theta_X) + \frac{1}{2}(|H_+|^2 + |H_-|^2)(1 + \cos^2\theta_X) \right] \\ &= \frac{3}{4} \left[f_L(1 - \cos^2\theta_X) + \frac{(1 - f_L)}{2}(1 + \cos^2\theta_X) \right], \end{aligned} \quad (3)$$

which is obtained from Eq. (2) via a definite integral over $\cos \theta_D$ and χ . Experimentally, the integral over $\cos \theta_D$ and χ must also include the acceptance in these angles. However, the acceptance is predominantly linear for both angles, as shown in Figs. 4 and 5, such that no significant residual dependence remains after the integration. Due to a common dependence on photon kinematics, the angle $\cos \theta_X$ and the invariant mass of the $D^{*-}D_s^+$ system are strongly negatively correlated, as illustrated in Appendix A in Fig. 7. More positive values of $\cos \theta_X$ correspond to higher momentum photons and thus lower values of $m(D^{*-}D_s^+)$. As a result, the different $\cos \theta_X$ shapes for longitudinal and transverse polarised $B^0 \rightarrow D^{*-}D_s^{*+}$ decays manifest in corresponding $m(D^{*-}D_s^+)$ distributions with different parabolic forms, as shown in Appendix A in Fig. 8. This feature enables f_L to be

measured using a binned maximum-likelihood fit to the $m(D^{*-}D_s^+)$ distribution in data, where the total $B^0 \rightarrow D^{*-}D_s^{*+}$ contribution is modelled by the sum of probability density functions (PDFs) for the longitudinal and transverse components with relative fractions f_L and $1 - f_L$. Determining f_L via an $m(D^{*-}D_s^+)$ fit enables partially reconstructed $B^0 \rightarrow D^{*-}D_s^{*+}$ decays to be used, which increases the sample size by avoiding efficiency losses due to the limited photon reconstruction efficiency of the LHCb detector.

Due to the presence of $B^0 \rightarrow D^{*-}D_s^+$ decays in the same sample, a measurement of the branching fraction ratio

$$\mathcal{R} \equiv \frac{\mathcal{B}(B^0 \rightarrow D^{*-}D_s^{*+}) \times \mathcal{B}(D_s^{*+} \rightarrow D_s^+\gamma)}{\mathcal{B}(B^0 \rightarrow D^{*-}D_s^+)} \quad (4)$$

can also be made. Experimentally, this quantity is defined as

$$\begin{aligned} \mathcal{R} &= \frac{\mathcal{N}(B^0 \rightarrow D^{*-}(D_s^{*+} \rightarrow D_s^+\gamma))}{\mathcal{N}(B^0 \rightarrow D^{*-}D_s^+)} \times \frac{\epsilon(B^0 \rightarrow D^{*-}D_s^+)}{\epsilon(B^0 \rightarrow D^{*-}(D_s^{*+} \rightarrow D_s^+\gamma))} \\ &= \frac{\mathcal{N}(B^0 \rightarrow D^{*-}(D_s^{*+} \rightarrow D_s^+\gamma))}{\mathcal{N}(B^0 \rightarrow D^{*-}D_s^+)} \times \xi, \end{aligned} \quad (5)$$

where \mathcal{N} denotes the yields for each decay mode, and ξ is the ratio of their total reconstruction and selection efficiencies. In the case of $B^0 \rightarrow D^{*-}D_s^{*+}$ decays, the yields and efficiencies correspond to those of partially reconstructed signal. The efficiency ratio is determined using simulated samples of $B^0 \rightarrow D^{*-}D_s^{*+}$ and $B^0 \rightarrow D^{*-}D_s^+$ decays, and is found to be $\xi = 1.142 \pm 0.034$, where the uncertainty quoted accounts only for the use of finite simulated samples and potential variation in the efficiency across data-taking years. This uncertainty is considered as a source of systematic uncertainty on \mathcal{R} .

A contribution from Cabibbo-suppressed $B_s^0 \rightarrow D^{*-}D_s^+$ decays is also considered in the $m(D^{*-}D_s^+)$ fit, enabling a measurement of the branching fraction ratio

$$r(B_s^0) \equiv \frac{\mathcal{B}(B_s^0 \rightarrow D^{*-}D_s^+)}{\mathcal{B}(B^0 \rightarrow D^{*-}D_s^+)} \quad (6)$$

to be made. Experimentally, $r(B_s^0)$ is defined as

$$\begin{aligned} r(B_s^0) &= \frac{f_d}{f_s} \times \frac{\mathcal{N}(B_s^0 \rightarrow D^{*-}D_s^+)}{\mathcal{N}(B^0 \rightarrow D^{*-}D_s^+)} \times \frac{\epsilon(B^0 \rightarrow D^{*-}D_s^+)}{\epsilon(B_s^0 \rightarrow D^{*-}D_s^+)} \\ &= \frac{f_d}{f_s} \times \frac{\mathcal{N}(B_s^0 \rightarrow D^{*-}D_s^+)}{\mathcal{N}(B^0 \rightarrow D^{*-}D_s^+)} \times \xi(B_s^0), \end{aligned} \quad (7)$$

where \mathcal{N} denotes the yields for each decay mode, and $f_s/f_d = 0.2539 \pm 0.0079$ is the ratio of fragmentation fractions at $\sqrt{s} = 13$ TeV as measured inside the LHCb acceptance [23]. The relative efficiency $\xi(B_s^0)$ is assumed to be unity, with a 5% relative systematic uncertainty assigned to account for potential variation in efficiency due to mass and lifetime differences.

5.1 Fit components

The $m(D^{*-}D_s^+)$ distribution of selected candidates is shown in Fig. 2, and is dominated by the narrow signal due to fully reconstructed $B^0 \rightarrow D^{*-}D_s^+$ decays and a broad structure due to $B^0 \rightarrow D^{*-}D_s^{*+}$ decays with missing a photon or π^0 from the D_s^{*+} decay. The distribution is modelled as a sum of several components which are described below.

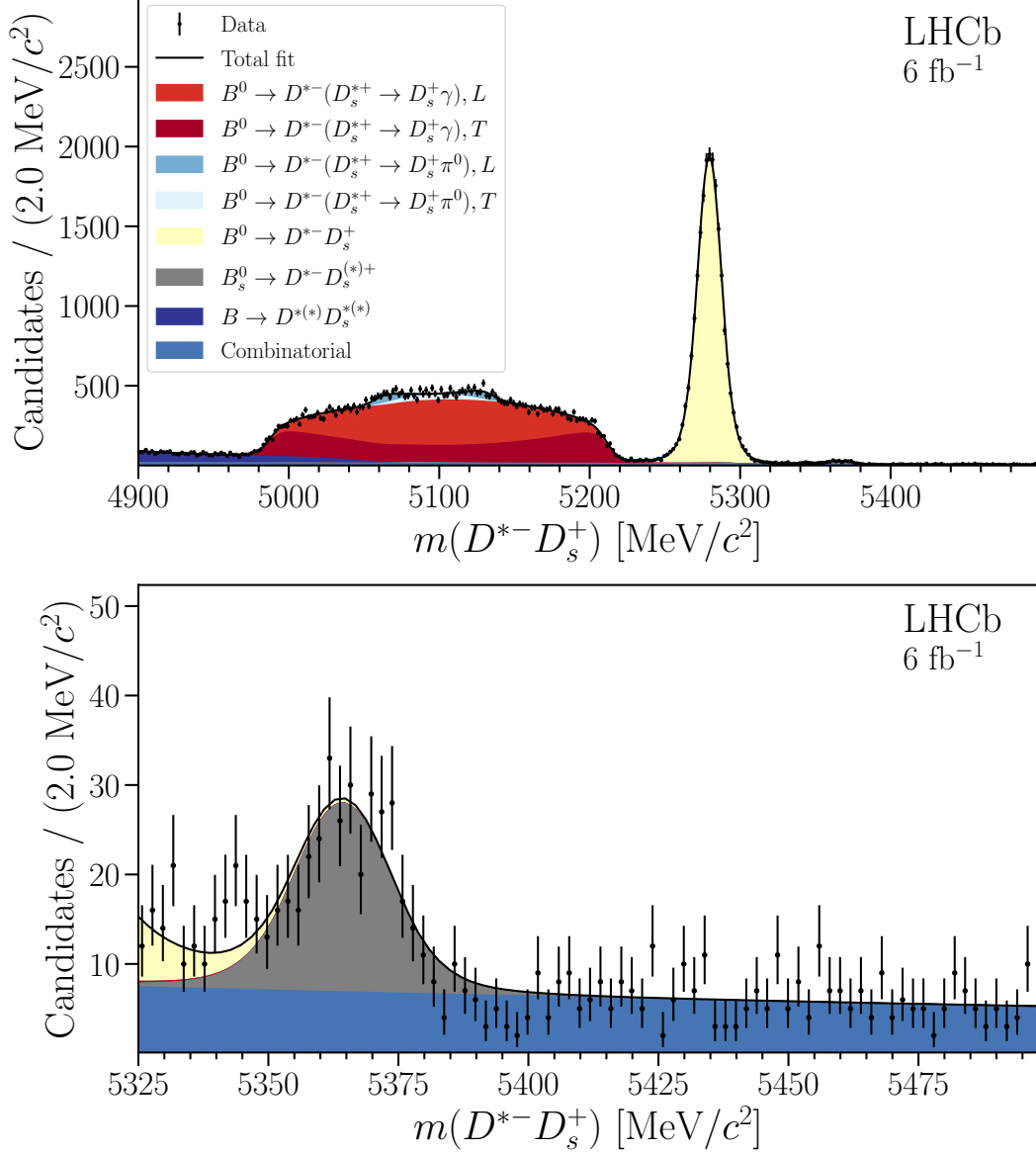


Figure 2: (Top) Distribution of $m(D^{*-}D_s^+)$ for selected candidates in data, with the fit overlaid. Where indicated, L (T) represents longitudinally (transverse) polarised decays. (Bottom) Restricted to region for candidates with $m(D^{*-}D_s^+) > 5325$ MeV/c², where the Cabibbo-suppressed $B_s^0 \rightarrow D^{*-}D_s^+$ contribution is visible.

$B^0 \rightarrow D^{*-}D_s^+$ decays

Fully reconstructed $B^0 \rightarrow D^{*-}D_s^+$ decays are modelled using the sum of two Crystal Ball PDFs [24] with a freely varying common mean and width, and a relative yield fraction that is Gaussian-constrained according to simulation. The component PDF tails are modelled on opposite sides, and the tail parameters are Gaussian-constrained from simulation. The branching fraction ratio \mathcal{R} is measured directly in the fit, such that the yield of the $B^0 \rightarrow D^{*-}D_s^+$ component is related to the yield of the $B^0 \rightarrow D^{*-}(D_s^{*+} \rightarrow D_s^+\gamma)$ component via a freely varying parameter \mathcal{R} and the fixed relative efficiency ratio ξ .

$B^0 \rightarrow D^{*-}(D_s^{*+} \rightarrow D_s^+\gamma)$ decays

The partially reconstructed $B^0 \rightarrow D^{*-}(D_s^{*+} \rightarrow D_s^+\gamma)$ signal is modelled using the sum of a longitudinal component and a transverse component, where a freely varying parameter f_L determines the relative proportion of the longitudinal component. To derive invariant-mass PDFs for each component, fits are performed to simulated samples of pure longitudinal and transverse polarised decays as shown in Appendix A in Fig. 9. The $m(D^{*-}D_s^+)$ distributions are modelled with parabolas convolved with Gaussian resolution functions, where the parabolas are based on the $\cos\theta_X$ dependence in Eq. (3). This approach closely follows the method used in Refs. [25] and [26] for CP violation studies of partially reconstructed $B^- \rightarrow D^{*0}h^-$ with $D^{*0} \rightarrow D\gamma/\pi^0$ decays, where h^- is a pion or a kaon and the neutral particle produced in the D^{*0} decay is not reconstructed. The total yield of the $B^0 \rightarrow D^{*-}(D_s^{*+} \rightarrow D_s^+\gamma)$ component, $\mathcal{N}(B^0 \rightarrow D^{*-}(D_s^{*+} \rightarrow D_s^+\gamma))$, varies freely and is used along with \mathcal{R} and ξ to set the $B^0 \rightarrow D^{*-}D_s^+$ component yield. All PDF parameters for the $B^0 \rightarrow D^{*-}(D_s^{*+} \rightarrow D_s^+\gamma)$ component are fixed in the data fit, and are varied within their uncertainties to determine the systematic uncertainties on f_L , \mathcal{R} , and $r(B_s^0)$.

$B^0 \rightarrow D^{*-}(D_s^{*+} \rightarrow D_s^+\pi^0)$ decays

A contribution from $B^0 \rightarrow D^{*-}(D_s^{*+} \rightarrow D_s^+\pi^0)$ decays, where the neutral pion from the D_s^{*+} decay is not reconstructed, is modelled in a similar manner to the $B^0 \rightarrow D^{*-}(D_s^{*+} \rightarrow D_s^+\gamma)$ signal. The contribution from this mode is small compared to the signal due to the lower branching fraction of the $D_s^{*+} \rightarrow D_s^+\pi^0$ decay [2]. To determine the invariant-mass PDF for this contribution, separate simulated samples of pure longitudinal and transverse decays are fitted with angular functions convolved with Gaussian resolution functions; all shape parameters are fixed in the data fit. The relative proportion of longitudinal and transverse decays is determined by f_L , where f_L is shared with the $B^0 \rightarrow D^{*-}(D_s^{*+} \rightarrow D_s^+\gamma)$ signal decay. The yield of this contribution is fixed relative to the $B^0 \rightarrow D^{*-}D_s^{*+}$ component using PDG D_s^{*+} branching fractions [2]. Both the fixed PDF parameters and branching fractions are varied within their uncertainties to determine the systematic uncertainty on f_L , \mathcal{R} , and $r(B_s^0)$.

Background from higher-excited charm states

At low $m(D^{*-}D_s^+)$ values, decays involving higher-excited charm states contribute when one or more particles are not reconstructed. To model the effective contribution from this feed-down background, simulated samples of $B^0 \rightarrow (D_1(2420)^- \rightarrow D^{*-}\pi^0)D_s^+$, $B^0 \rightarrow D^{*-}(D_{s1}(2460)^+ \rightarrow D_s^+\gamma)$, $B^0 \rightarrow D^{*-}(D_{s1}(2460)^+ \rightarrow (D_s^{*+} \rightarrow D_s^+\gamma)\pi^0)$, and $B^0 \rightarrow (D_1(2420)^- \rightarrow D^{*-}\pi^0)(D_s^{*+} \rightarrow D_s^+\gamma)$ decays generated using RAPIDSIM are studied. The $D_1(2420)^-$ modes are taken as a proxy to represent contributions from similar decays involving $D_1(2430)^-$ and $D_2^*(2460)^-$ mesons, and decays involving two higher-excited charm states are expected to be negligibly small. Invariant-mass fits to simulated events in the 4900–5350 MeV/ c^2 region are performed using sums of several parabolas convolved with resolution functions, where all shape parameters are subsequently fixed in the data fit and varied within their uncertainties to determine the systematic uncertainty. Polarised decays involving two vector mesons are generated using the world-average value of f_L in $B^0 \rightarrow D^{*-}D_s^{*+}$ decays [2]. Alternative samples are generated with a $\pm 20\%$ variation in f_L to evaluate the change in PDF shape parameters, and the

differences observed are assigned as a source of systematic uncertainty. The degree of variation introduced in f_L is motivated by comparing the polarisation fractions measured in several $\bar{B}^0 \rightarrow D\omega$ decays, where $D \in \{D^{*0}, D_1(2420)^0, D_1(2430)^0, D_2^*(2460)^0\}$ [2]. The yields of each feed-down contribution are Gaussian-constrained relative to the $B^0 \rightarrow D^{*-}D_s^+$ yield using a product of PDG branching fractions [2], efficiencies for the $m(D^{*-}D_s^+)$ mass window requirement taken from simulation, and a factor of two to account for the similar expected contributions from B^\pm decays. An additional factor of 0.20 ± 0.04 is included for the $D_1(2420)^-D_s^{(*)+}$ modes, in order to model the $B \rightarrow (\bar{D}^{**} \rightarrow D^{*-}X)D_s^{(*)+}$ rate relative to $B \rightarrow D^{*-}D_s^{(*)+}$. This factor is motivated by control mode studies of the rate of $B^+ \rightarrow D^{*-}D_s^+\pi^+$ decays relative to $B^0 \rightarrow D^{*-}D_s^+$ decays.

Combinatorial background

Background from random track combinations is modelled using an exponential function with a freely varying shape parameter and yield. Due to the application of mass windows for the charm-meson candidates and a D_s^+ candidate flight requirement, the combinatorial background is found to be small across the full $m(D^{*-}D_s^+)$ range considered.

Contributions from B_s^0 decays

The contribution from Cabibbo-suppressed $B_s^0 \rightarrow D^{*-}D_s^+$ decays falls at higher $m(D^{*-}D_s^+)$ values than the $B^0 \rightarrow D^{*-}D_s^+$ decay due to the larger mass of the B_s^0 meson. This decay is modelled using the same PDF parameterisation as the $B^0 \rightarrow D^{*-}D_s^+$ peak, but with independent and freely varying mean and width parameters. The branching fraction ratio $r(B_s^0)$ varies freely in the fit, such that the $B_s^0 \rightarrow D^{*-}D_s^+$ yield is determined by $r(B_s^0)$, $\xi(B_s^0)$, and the external value of f_s/f_d .

Partially reconstructed $B_s^0 \rightarrow D^{*-}D_s^{*+}$ decays are modelled using the same parameterisation as that for $B^0 \rightarrow D^{*-}D_s^{*+}$ decays, but with an upward shift in mass set using the known B_s^0 - B^0 meson mass difference. The rate of this contribution is determined relative to the $B^0 \rightarrow D^{*-}D_s^{*+}$ component using the ratio of the $B_s^0 \rightarrow D^{*-}D_s^{*+}$ and $B^0 \rightarrow D^{*-}D_s^{*+}$ component yields, with an additional Gaussian-constrained factor of 1.00 ± 0.33 included to allow for potential differences between the $B_s^0 \rightarrow D^{*-}D_s^{*+}$ and $B_s^0 \rightarrow D^{*-}D_s^+$ decay rates over a range 0–2. The longitudinal polarisation fraction of the $B_s^0 \rightarrow D^{*-}D_s^{*+}$ component is Gaussian constrained to the value 0.52 ± 0.16 based on the world average value for $B^0 \rightarrow D^{*-}D_s^{*+}$ decays [1, 2], where the permitted variation allows for f_L values in the range 0–1.

5.2 Results

The fit to the $m(D^{*-}D_s^+)$ distribution in data is shown in Fig. 2, where candidates with $m(D^{*-}D_s^+) > 5325 \text{ MeV}/c^2$ are shown on a separate y -axis scale in order to highlight the $B_s^0 \rightarrow D^{*-}D_s^+$ peak. Yields of $\mathcal{N}(B^0 \rightarrow D^{*-}(D_s^{*+} \rightarrow D_s^+\gamma)) = 37415 \pm 361$, $\mathcal{N}(B^0 \rightarrow D^{*-}D_s^+) = 20890 \pm 178$, and $\mathcal{N}(B_s^0 \rightarrow D^{*-}D_s^+) = 261 \pm 30$ are obtained, where the uncertainties quoted are statistical only. Studies with pseudoexperiments indicate that the central values and uncertainties of the yields are unbiased. The ratio of branching fractions of $B^0 \rightarrow D^{*-}(D_s^{*+} \rightarrow D_s^+\gamma)$ decays relative to $B^0 \rightarrow D^{*-}D_s^+$ decays is measured

to be

$$\mathcal{R} = 2.045 \pm 0.022 \pm 0.071,$$

where the first uncertainty is statistical and the second is systematic. In addition, the ratio of branching fractions of the Cabibbo-suppressed $B_s^0 \rightarrow D^{*-}D_s^+$ decay relative to the $B^0 \rightarrow D^{*-}D_s^+$ decay is measured to be

$$r(B_s^0) = 0.049 \pm 0.006 \pm 0.003 \pm 0.002,$$

where the first uncertainty is statistical, the second is systematic, and the third is due to the use of an external value of f_s/f_d [23]. The systematic uncertainties on \mathcal{R} and $r(B_s^0)$ are due to the use of fixed PDF shape parameters and branching fractions in the fit, as well as the use of the relative efficiency corrections ξ and $\xi(B_s^0)$. The contributing systematic uncertainties on both branching fraction ratios are summarised in Table 1 in Sect. 9. The value of \mathcal{R} is in agreement with the world average, $\mathcal{R} = 2.07 \pm 0.33$, but has a considerably smaller uncertainty. The measurement of $r(B_s^0)$ is a world first, and constitutes the first observation of the Cabibbo-suppressed $B_s^0 \rightarrow D^{*-}D_s^+$ decay with a statistical significance of seven standard deviations. The significance is calculated by determining the difference in $r(B_s^0)$ from zero, where both the statistical and systematic uncertainties are considered.

The longitudinal polarisation fraction in $B^0 \rightarrow D^{*-}(D_s^{*+} \rightarrow D_s^+\gamma)$ decays is measured to be

$$f_L = 0.578 \pm 0.010 \pm 0.011,$$

where the first uncertainty is statistical and the second is systematic. The systematic uncertainty quoted is due to the limited knowledge of the fixed terms used in the fit. This result is in agreement with, but substantially more precise than, the current world-average value. Pseudoexperiment studies indicate that the fitted central value and uncertainty of f_L are unbiased. In the subsequent analysis of fully reconstructed $B^0 \rightarrow D^{*-}D_s^{*+}$ decays presented herein, f_L is fixed to the value measured in the $m(D^{*-}D_s^+)$ fit. This enables the angular acceptance functions for $\cos\theta_D$ and $\cos\theta_X$ to be derived directly from data (see Sect. 7), rather than modelling such effects using simulation. The $\cos\theta_X$ distribution in particular is sensitive to mis-modelling in the simulation, due to its dependence on the soft photon kinematics which can be distorted by the hardware trigger emulation in the simulation.

6 Invariant-mass fit to $B^0 \rightarrow D^{*-}D_s^{*+}$ decays

To derive signal weights for the angular analysis, a binned maximum-likelihood fit to the $m(D^{*-}D_s^{*+})$ distribution of fully reconstructed $B^0 \rightarrow D^{*-}D_s^{*+}$ candidates in data is performed using the *sPlot* method [27]. The $m(D^{*-}D_s^{*+})$ distribution is shown in Fig. 3, where the fit is overlaid. This fully reconstructed sample contains 17% of the candidates used in the $m(D^{*-}D_s^+)$ fit in Sect. 5; the smaller sample size is attributed to the limited soft photon reconstruction efficiency, and the application of additional requirements on the photon and D_s^{*+} candidate. Potential background contributions from $B^0 \rightarrow D^{*-}D_s^{*+}$ decays with $D_s^{*+} \rightarrow D_s^+\pi^0$ are determined to be negligible within the window of $D_s^{*+}-D_s^+$ mass difference considered.

The fit is performed using the sum of a $B^0 \rightarrow D^{*-}(D_s^{*+} \rightarrow D_s^+ \gamma)$ signal component, a $B_s^0 \rightarrow D^{*-}(D_s^{*+} \rightarrow D_s^+ \gamma)$ background component, and a combinatorial background component. The signal is described using the sum of two Crystal Ball PDFs which share a common freely varying mean and width. The tail parameters and relative fraction of the two Crystal Ball PDFs are constrained from fits to simulation, where the component PDFs are required to have tails on opposite sides. The yield of the signal component varies freely, and is found to be 6457 ± 116 . The $B_s^0 \rightarrow D^{*-}(D_s^{*+} \rightarrow D_s^+ \gamma)$ component is modelled using the same PDF as the signal, but with a mean shifted upwards using the known B_s^0 - B^0 meson mass difference. The rate of this contribution is fixed relative to signal using the proportions determined in the $m(D^{*-}D_s^+)$ fit. The combinatorial background is modelled using a second-order Chebyshev polynomial, where the yield and shape parameters of this contribution vary freely. As the background distribution is not known a priori, an alternative parameterisation using a Gaussian function is also used to model the combinatorial background. The signal weights derived from this alternative model are used to determine the systematic uncertainty on the helicity observables. A Gaussian function is used as it provides a background description of equivalent quality to the second-order Chebyshev, whereas linear and exponential background models do not describe the background sufficiently well.

An underlying assumption of the *sPlot* method used to derive per-candidate signal weights is that the discriminating variable, in this case $m(D^{*-}D_s^{*+})$, is uncorrelated with the target distributions to be studied with weights applied, in this instance the decay angles. Due to a common underlying dependence on the decay product kinematics, the invariant mass and decay angles do exhibit some degree of correlation. To assess the potential bias from this, a combined four-dimensional simulated sample of signal and background events is generated in $m(D^{*-}D_s^{*+})$ and the decay angles. The background sample is generated according to the $m(D^{*-}D_s^{*+})$ background shape observed in data, and with a flat distribution in each of the decay angles. The total simulated sample contains the same number of signal and background events as measured in the $m(D^{*-}D_s^{*+})$ data fit. A fit to the $m(D^{*-}D_s^{*+})$ distribution of the simulated sample is performed to derive signal weights, which are then applied when creating histograms in the decay angles. Using χ^2 tests, these histograms are compared to histograms of the decay angles created using only the simulated signal sample. All of the signal-weighted distributions are found to agree with the pure signal distributions, indicating that no significant biases are incurred from the use of signal weights.

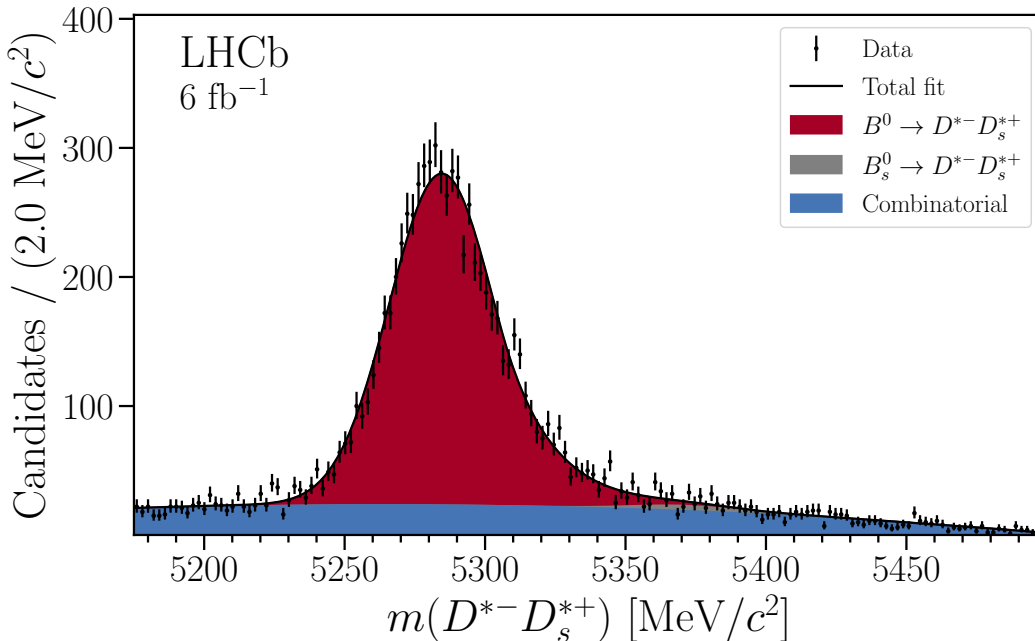


Figure 3: Distribution of $m(D^{*-}D_s^{*+})$ for selected candidates in data, with the fit overlaid.

7 Angular acceptance functions

Due to experimental acceptance and resolution effects, the angular distributions in data are distorted relative to the true distributions. As the decay angles are measured with a relative resolution of 2–4% according to simulation, the dominant effect on the experimental angular distributions is due to the acceptance. This effect must be modelled in the angular fit in order to derive unbiased measurements of the helicity observables, which is achieved by multiplying the true differential decay rate PDF by acceptance functions defined in each of the decay angles. This approach assumes that the total angular acceptance can be factorised into a product of the individual acceptance functions for each angle, which is validated using a simulated sample of signal decays generated according to Eq. (2) with the world-average value of $f_L = 0.52$ [1, 2], $|H_+| = |H_-| = \sqrt{(1 - f_L)/2}$, and all phases equal to zero. The efficiency of a cut applied to all three decay angles together, ϵ_{xyz} , is compared with a product of the efficiencies for cuts applied separately to each decay angle, $\epsilon' = \epsilon_x \times \epsilon_y \times \epsilon_z$; the values of ϵ_{xyz} and ϵ' are found to agree within the uncertainties due to the use of finite simulated samples.

7.1 Acceptance functions for $\cos\theta_D$ and $\cos\theta_X$

The acceptance functions for $\cos\theta_D$ and $\cos\theta_X$ are derived from data. Binned normalised distributions in each decay angle are produced by creating histograms of the fully reconstructed $B^0 \rightarrow D^{*-}D_s^{*+}$ candidates in data with signal weights applied. The only physical observable that can alter the shape of the one-dimensional $\cos\theta_D$ and $\cos\theta_X$ distributions is f_L , which is known from the $m(D^{*-}D_s^{*+})$ fit. The acceptance is thus determined by comparing the data distributions with angular distributions generated with RAPIDSIM

using the value of f_L measured in Sect. 5. In the generated sample, no detector acceptance or resolution effects are included. The signal-weighted data and generated signal distributions in $\cos\theta_D$ and $\cos\theta_X$ are compared in Fig. 4 (left column). The observed differences between data and the generated sample are attributed to the experimental acceptance and resolution, since both distributions share a common f_L value. The $\cos\theta_X$ distribution in particular exhibits substantial acceptance effects, where candidates at low $\cos\theta_X$ are preferentially removed. This warping is due to the application of photon p_T requirements in the selection, which bias the sample to more positive values of $\cos\theta_X$.

To determine acceptance functions for $\cos\theta_D$ and $\cos\theta_X$, the binned ratios of data to the generated sample are fitted with sixth-order polynomial functions. The fits are shown in Fig. 4 (right column), and the polynomial coefficients are employed as fixed terms in the angular fit in Sect. 8. To determine the systematic uncertainty on the helicity observables due to the finite dataset used in the acceptance fits, the acceptance function coefficients are varied within their uncertainties according to the acceptance fit covariance matrices. When determining the systematic uncertainty due to the use of a fixed f_L value in the angular analysis, the acceptance fits are performed many times with f_L varied randomly within its total measured uncertainty.

For values of $\cos\theta_X$ close to -1 , which correspond to the smallest photon momentum values, the acceptance function becomes slightly negative due to limited data statistics in this region. A fiducial cut of $\cos\theta_X > -0.9$ is applied to data in order to remove the region of negative modelled acceptance; this requirement is found to have a negligible impact on the measured helicity observables.

7.2 Acceptance function for χ

In Eq. (2), all of the angular terms that are sensitive to the relative magnitudes and phases of the transverse amplitudes have a dependence on the angle χ . As such, no information on the χ acceptance can be derived from data. To determine the χ acceptance, the reconstructed χ distribution in a sample of fully-simulated $B^0 \rightarrow D^{*-} D_s^{*+}$ decays passing all selection requirements is compared to a generated χ distribution produced using RAPIDSIM with the same model parameters but no acceptance or resolution effects. For this comparison, the simulated samples are generated with the f_L value measured in Sect. 5, with $|H_-| = |H_+|$ and $\phi_+ = \phi_- = 0$. The binned χ distributions are shown in Fig. 5 (left), where good agreement between the reconstructed and generated distributions is found. This indicates that the reconstructed χ distribution is not strongly modified by acceptance effects. To model residual acceptance effects, the reconstructed to generated χ ratio is fitted with a second-order polynomial, as shown in Fig. 5 (right). This function is employed as a fixed correction PDF in the angular fit, and the polynomial coefficients are varied within their uncertainties to determine the systematic uncertainties on the helicity parameters. In this procedure, the correlations between the polynomial coefficients are accounted for using the acceptance fit covariance matrix.

8 Angular fit to data

To measure $|H_-|$, ϕ_- , and ϕ_+ , an unbinned maximum-likelihood fit to the three-dimensional angular distribution of signal-weighted data is performed using ZFIT [28]. For the fit,

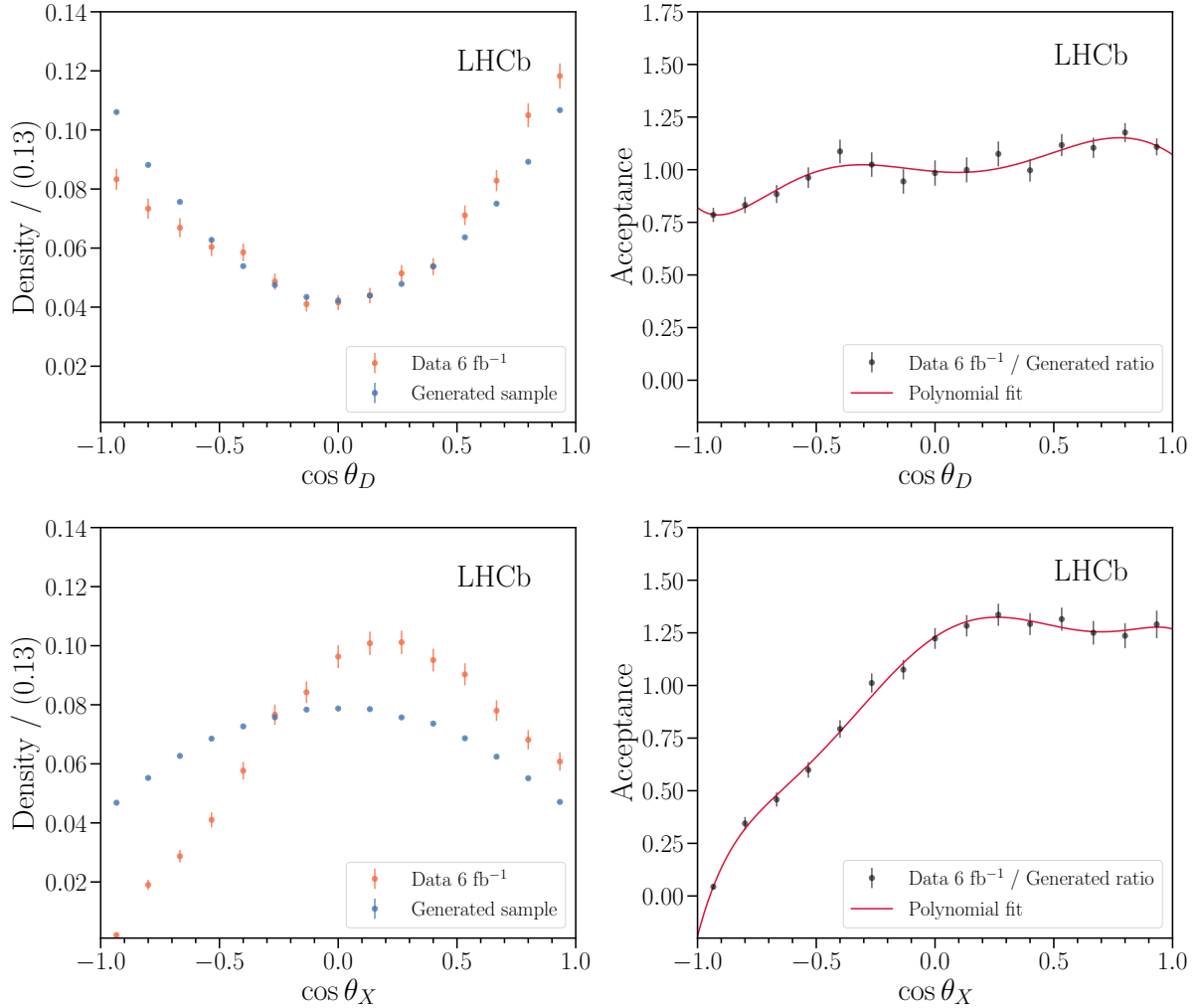


Figure 4: (Left) Comparison of signal-weighted data and generated (top) $\cos \theta_D$ and (bottom) $\cos \theta_X$ distributions, where the differences observed are due to the experimental acceptance and resolution. (Right) Data to generated sample ratios, with the polynomial fits overlaid.

the $B^0 \rightarrow D^{*-}(D_s^{*+} \rightarrow D_s^+ \gamma)$ candidates from the $m(D^{*-}D_s^{*+})$ fit in Sect. 6 are used with per-candidate signal weights assigned. The longitudinal polarisation amplitude, H_0 , is assigned a fixed magnitude $|H_0|$ using the value of f_L measured in Sect. 5, and its phase is set to the arbitrary value $\phi_0 = 0$. The parameter $|H_+|$ is fully determined by the normalisation of the helicity amplitudes to unity. The signal density at each point in angular phase space is described using Eq. (2) multiplied by acceptance functions in each of the decay angles. To determine the statistical uncertainties of the observables, the fit applies an asymptotic correction to the covariance matrix as detailed in Ref. [29], which correctly accounts for the use of signal-weighted data. The distributions for each decay angle are shown in Fig. 6, with the one-dimensional fit projections overlaid.

Studies with pseudoexperiments are performed to determine the level of bias present in the results, where pull distributions of mean μ_P^x and width σ_P^x are constructed for each observable x . The pull distributions for each helicity observable are found to follow Gaussian distributions closely, where $\sigma_P^{|H_-|}$ is consistent with unity. However,

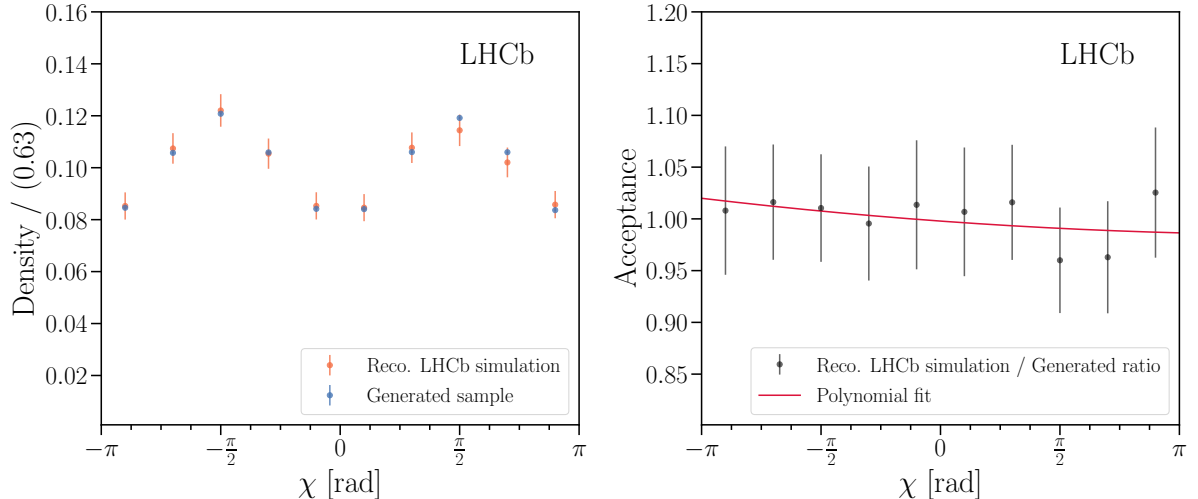


Figure 5: Comparison of reconstructed χ distribution in a fully-simulated $B^0 \rightarrow D^{*-} D_s^{*+}$ sample and the generated χ distribution in a RAPIDSIM sample produced with the same helicity amplitude model (left). The ratio is fitted with a second-order polynomial to determine the acceptance function for use in the data fit (right).

$\sigma_P^{\phi^+} = 1.14 \pm 0.02$ and $\sigma_P^{\phi^-} = 1.12 \pm 0.02$, indicating that the default fit uncertainties for these observables are underestimated. The mean values of the pulls for the transverse phases are consistent with zero, but $\mu_P^{|H^-|} = -0.14 \pm 0.02$. These biases are traced to the finite size of the fitted dataset, and are found to resolve when pseudoexperiment datasets containing more events than are present in data are generated. The values of μ_P^x and σ_P^x are used to correct the default fit results $x \pm \sigma_x$ as follows

$$x^c = x - \mu_P^x \times \sigma_x \quad (8)$$

$$\sigma_x^c = \sigma_P^x \times \sigma_x \quad (9)$$

where $x^c \pm \sigma_x^c$ are the corrected fit results. In Sect. 10, the results for $|H_-|$, ϕ_+ , and ϕ_- are quoted after this correction procedure.

9 Systematic uncertainties

The values of \mathcal{R} , $r(B_s^0)$, and f_L measured in Sect. 5 are subject to systematic uncertainties due to limited knowledge of the shape parameters, branching fractions, and relative efficiency corrections used in the fit. To determine these systematic uncertainties, the $m(D^{*-} D_s^+)$ fit to data is performed many times with the parameters randomly varied within their prescribed uncertainties according to Gaussian distributions. This procedure is performed separately for the shape parameters, branching fractions, and efficiency corrections, and the total systematic uncertainties calculated as the sum in quadrature of these contributions. The systematic uncertainties are summarised in Table 1.

The observables $|H_-|$, ϕ_+ , and ϕ_- measured in the angular fit are subject to several systematic uncertainties. Firstly, the angular analysis is performed at a fixed value of f_L , which is used as input in the $\cos\theta_D$ and $\cos\theta_X$ acceptance fits and also to set the

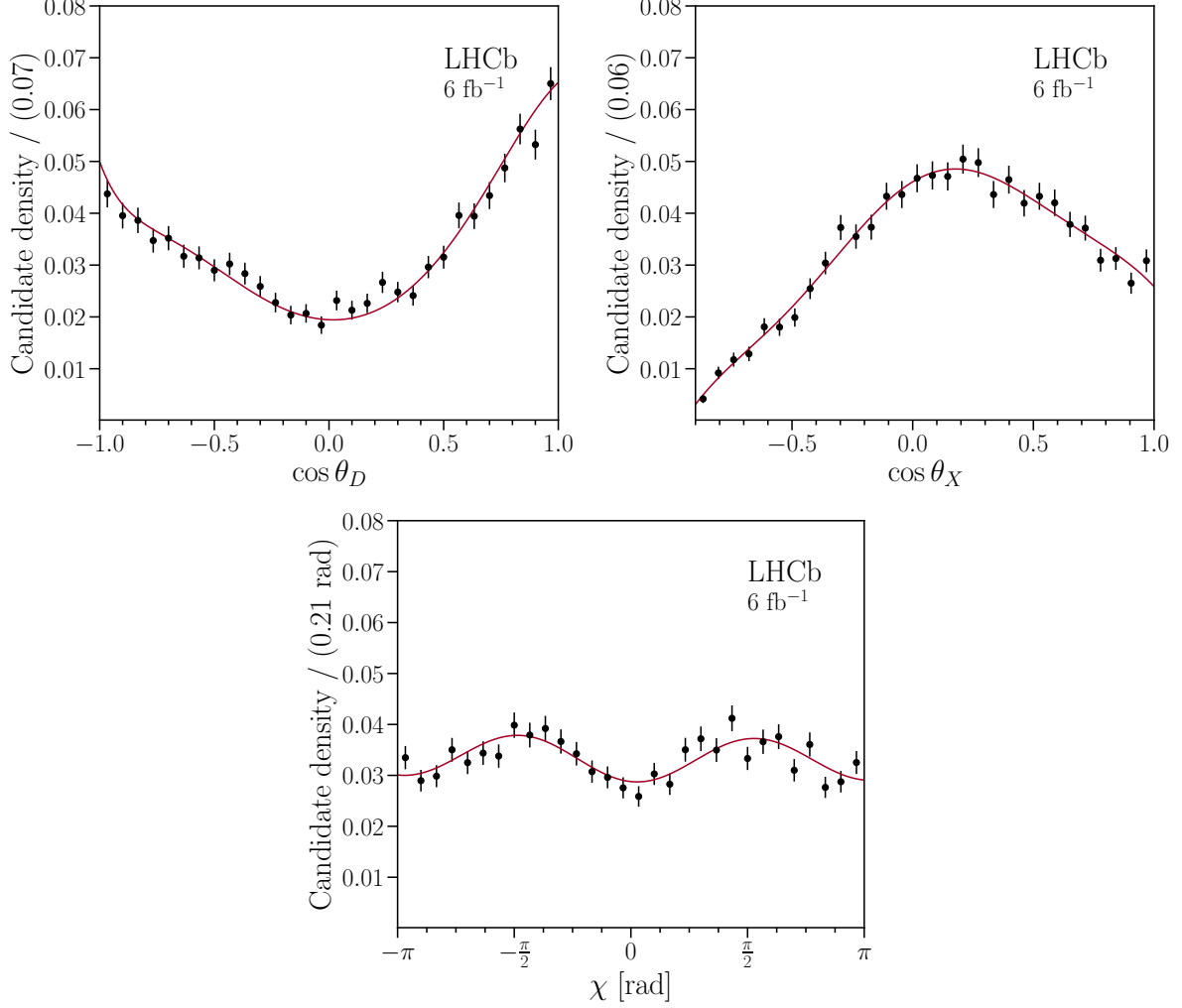


Figure 6: Decay-angle distributions of signal-weighted $B^0 \rightarrow D^{*-}D_s^{*+}$ candidates in data, with the one-dimensional angular fit projections overlaid.

value of $|H_0|$ in the angular fit. To determine the systematic uncertainty, the angular analysis is repeated many times with f_L varied within its total uncertainty; the standard deviations of the helicity observable results are taken as the systematic uncertainties. In this procedure, the varied f_L value used in the acceptance fits is shared with the angular fit to ensure consistency. A small systematic uncertainty is also assigned for the use of signal-weighted data, where the angular fit is run many times while varying the signal weights within the signal yield uncertainties from the $m(D^{*-}D_s^{*+})$ fit. To determine the systematic uncertainty from the use of finite samples to obtain the acceptance functions, the acceptance coefficients are varied within their uncertainties according to the acceptance fit covariance matrices. Finally, the angular analysis is repeated with an alternative background model in the $m(D^{*-}D_s^{*+})$ fit, and the differences in central value for each helicity observable are assigned as a systematic uncertainty. The contributing systematic uncertainties are summarised in Table 2.

Table 1: Systematic uncertainties on the branching fraction ratios and f_L as measured in the $m(D^{*-}D_s^+)$ fit.

| Systematic uncertainty | \mathcal{R} | $\mathcal{R}(B_s^0)$ | f_L |
|----------------------------|---------------|----------------------|--------|
| Fixed PDF shape parameters | 0.030 | 0.00197 | 0.0074 |
| Fixed branching fractions | 0.016 | 0.00004 | 0.0080 |
| Efficiency corrections | 0.062 | 0.00253 | 0.0001 |
| Total | 0.071 | 0.00320 | 0.0109 |

Table 2: Systematic uncertainties on the helicity parameters measured in the unbinned angular fit.

| Systematic uncertainty | $ H_- $ | ϕ_+ | ϕ_- |
|--|---------|----------|----------|
| Fixed f_L in angular fit and $\cos(\theta_{X/D})$ acceptance | 0.0005 | 0.0007 | 0.005 |
| Use of $_s$ Weighted data | 0.0003 | 0.0011 | 0.002 |
| Statistical uncertainty of acceptance functions | 0.0034 | 0.0132 | 0.044 |
| $m(D^*D_s^*)$ fit background model | 0.0319 | 0.0156 | 0.025 |
| Total | 0.0321 | 0.0205 | 0.051 |

10 Results and conclusion

Using a fit to the $m(D^{*-}D_s^+)$ distribution to determine the properties of partially reconstructed $B^0 \rightarrow D^{*-}(D_s^{*+} \rightarrow D_s^+\gamma)$ decays, the longitudinal polarisation fraction is measured to be

$$f_L = 0.578 \pm 0.010 \pm 0.011,$$

where the first uncertainty is statistical and the second is systematic. The corresponding magnitude of the longitudinal helicity amplitude, given by $|H_0| = \sqrt{f_L}$, is

$$|H_0| = 0.760 \pm 0.007 \pm 0.007.$$

This information is used to measure the remaining helicity observables in an angular fit to fully reconstructed $B^0 \rightarrow D^{*-}(D_s^{*+} \rightarrow D_s^+\gamma)$ decays, obtaining

$$\begin{aligned} |H_-| &= 0.195 \pm 0.022 \pm 0.032, \\ |H_+| &= 0.620 \pm 0.011 \pm 0.013, \\ \phi_+ &= -0.046 \pm 0.102 \pm 0.020, \\ \phi_- &= 0.108 \pm 0.170 \pm 0.051, \end{aligned}$$

where the quoted value and uncertainties for $|H_+|$ are fully determined by the normalisation of the three helicity amplitudes to unity. The measurement of f_L is consistent with and more precise than the current world average, $f_L = 0.52 \pm 0.05$ [1, 2]. The transverse amplitude magnitudes and phases are measured for the first time, where both phases are consistent with zero but the magnitudes differ from each other at the level of nine standard

deviations. It is noted that $|H_0| > |H_+| > |H_-|$, which is expected from quark-helicity conservation in B decays involving a $b \rightarrow c$ quark transition. In such decays, the $V - A$ nature of the weak interaction causes the longitudinal component to dominate. The inequality is stronger for decays involving light vector mesons [7], but also appears to be satisfied in $B^0 \rightarrow D^{*-} D_s^{*+}$ decays where two vector charm mesons are produced. This helicity hierarchy is not observed in decays dominated by penguin amplitudes such as $B^0 \rightarrow \phi K^{*0}$, where the longitudinal and transverse components are found to have roughly equal amplitudes [30–33].

The branching fraction ratio of $B^0 \rightarrow D^{*-}(D_s^{*+} \rightarrow D_s^+ \gamma)$ decays relative to $B^0 \rightarrow D^{*-} D_s^+$ decays is measured to be

$$\mathcal{R} = 2.045 \pm 0.022 \pm 0.071,$$

where the first uncertainty is statistical and the second is systematic. This result is in agreement with, but considerably more precise than, the current world-average value $\mathcal{R} = 2.07 \pm 0.33$ [2]. The branching fraction ratio of the Cabibbo-suppressed $B_s^0 \rightarrow D^{*-} D_s^+$ decay relative to the $B^0 \rightarrow D^{*-} D_s^+$ decay is measured to be

$$r(B_s^0) = 0.049 \pm 0.006 \pm 0.003 \pm 0.002,$$

where the first uncertainty is statistical, the second is systematic, and the third accounts for the use of an external value of f_s/f_d [23]. This measurement constitutes the first observation of the Cabibbo-suppressed $B_s^0 \rightarrow D^{*-} D_s^+$ decay with a significance of seven standard deviations.

In conclusion, an angular analysis of $B^0 \rightarrow D^{*-} D_s^{*+}$ with $D_s^{*+} \rightarrow D_s^+ \gamma$ decays is performed using 6 fb^{-1} of data collected with the LHCb experiment at $\sqrt{s} = 13 \text{ TeV}$ in order to measure a complete set of helicity amplitude observables. Partially reconstructed candidates are used in a fit to the $m(D^{*-} D_s^+)$ distribution to measure the longitudinal polarisation fraction $f_L = |H_0|^2$. This knowledge is then used in a subsequent angular fit to fully reconstructed data in order to measure the remaining helicity observables. The measurement of f_L is consistent with and more precise than the current world-average value, while the magnitudes and phases of the transverse helicity amplitudes are measured for the first time. The pattern of helicity amplitude magnitudes is found to align with expectations from quark-helicity conservation for tree-level B decays involving a $b \rightarrow c$ transition. The $B^0 \rightarrow D^{*-} D_s^{*+}$ decay is a large background in $B^0 \rightarrow D^{*-} \tau^+ \nu_\tau$ analyses, particularly when the τ^+ decays hadronically. Analyses aiming to measure angular observables in $B^0 \rightarrow D^{*-} \tau^+ \nu_\tau$ decays must control the angular distributions of prominent hadronic backgrounds such as $B^0 \rightarrow D^{*-} D_s^{*+}$, and the results presented herein will help to significantly reduce background model uncertainties in future measurements.

Acknowledgements

We express our gratitude to our colleagues in the CERN accelerator departments for the excellent performance of the LHC. We thank the technical and administrative staff at the LHCb institutes. We acknowledge support from CERN and from the national agencies: CAPES, CNPq, FAPERJ and FINEP (Brazil); MOST and NSFC (China); CNRS/IN2P3 (France); BMBF, DFG and MPG (Germany); INFN (Italy); NWO (Netherlands); MNiSW

and NCN (Poland); MEN/IFA (Romania); MSHE (Russia); MICINN (Spain); SNSF and SER (Switzerland); NASU (Ukraine); STFC (United Kingdom); DOE NP and NSF (USA). We acknowledge the computing resources that are provided by CERN, IN2P3 (France), KIT and DESY (Germany), INFN (Italy), SURF (Netherlands), PIC (Spain), GridPP (United Kingdom), RRCKI and Yandex LLC (Russia), CSCS (Switzerland), IFIN-HH (Romania), CBPF (Brazil), PL-GRID (Poland) and NERSC (USA). We are indebted to the communities behind the multiple open-source software packages on which we depend. Individual groups or members have received support from ARC and ARDC (Australia); AvH Foundation (Germany); EPLANET, Marie Skłodowska-Curie Actions and ERC (European Union); A*MIDEX, ANR, IPhU and Labex P2IO, and Région Auvergne-Rhône-Alpes (France); Key Research Program of Frontier Sciences of CAS, CAS PIFI, CAS CCEPP, Fundamental Research Funds for the Central Universities, and Sci. & Tech. Program of Guangzhou (China); RFBR, RSF and Yandex LLC (Russia); GVA, XuntaGal and GENCAT (Spain); the Leverhulme Trust, the Royal Society and UKRI (United Kingdom).

Appendices

A Relationship between $m(D^{*-}D_s^+)$ and $\cos\theta_X$

In Fig. 7, the relationship between $m(D^{*-}D_s^+)$ and $\cos\theta_X$ is shown for fully reconstructed $B^0 \rightarrow D^{*-}(D_s^{*+} \rightarrow D_s^+\gamma)$ simulated decays. A strong negative correlation is evident, due to a common dependence on the kinematics of the photon produced in the D_s^{*+} decay. The one-dimensional decay rate as a function of $\cos\theta_X$ is given by Eq. (3), where separate transverse and longitudinal components contribute; these components are illustrated in Fig. 8. Due to the co-dependence of $m(D^{*-}D_s^+)$ and $\cos\theta_X$, the different angular forms for transverse and longitudinal signal give rise to different $m(D^{*-}D_s^+)$ distributions. This is illustrated in Fig. 9, where RAPIDSIM samples of transverse and longitudinal signal are shown. The fits used to derive shape parameters for the $m(D^{*-}D_s^+)$ fit are overlaid.

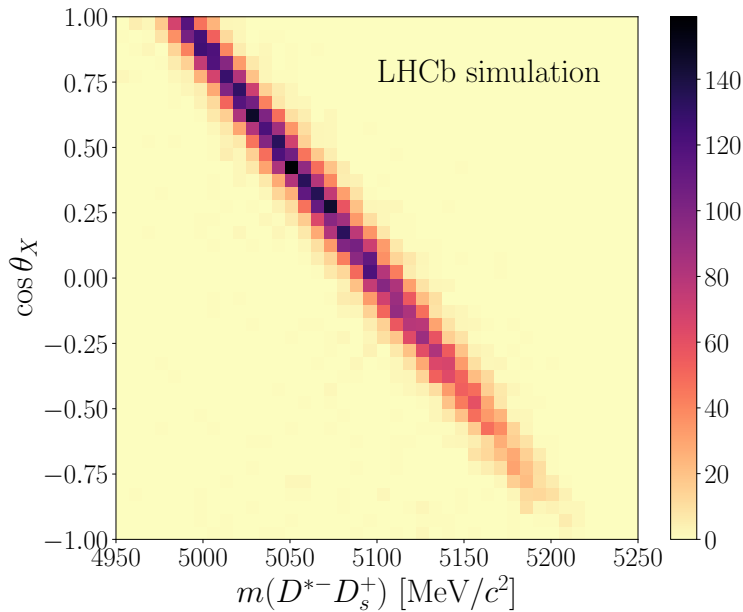


Figure 7: Relationship between $m(D^{*-}D_s^+)$ and $\cos\theta_X$ in a sample of fully reconstructed $B^0 \rightarrow D^{*-}(D_s^{*+} \rightarrow D_s^+\gamma)$ simulated decays. The colour scale indicates the number of candidates in each bin.

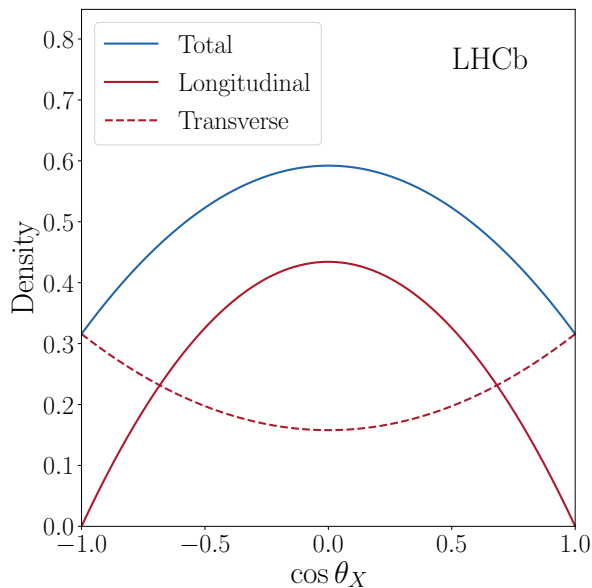


Figure 8: Transverse and longitudinal contributions to the one-dimensional decay rate shown as a function of $\cos \theta_X$.

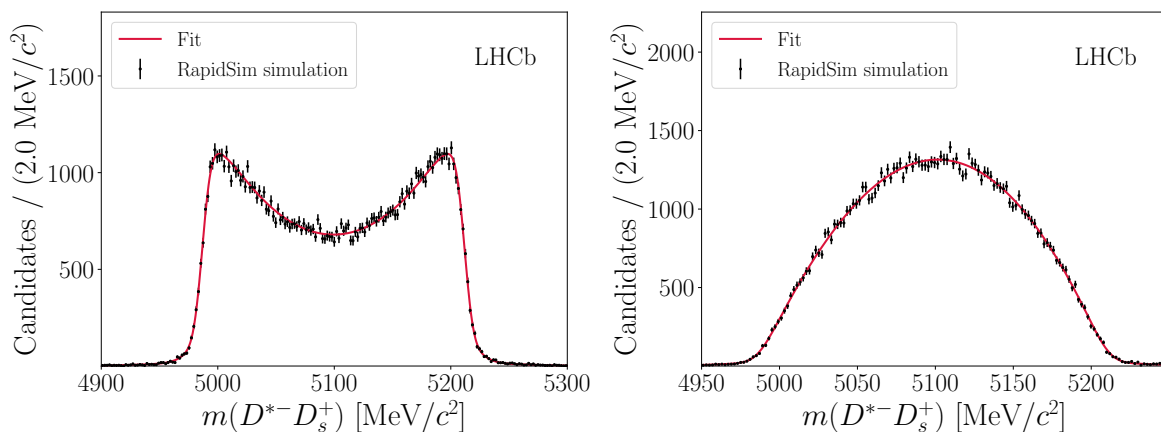


Figure 9: Invariant-mass distributions of (left) pure transverse and (right) longitudinal $B^0 \rightarrow D^{*-} (D_s^{*+} \rightarrow D_s^+ \gamma)$ simulated decays. Fits to the distributions are overlaid, from which shape parameters for use in the $m(D^{*-} D_s^+)$ data fit are derived.

References

- [1] BaBar collaboration, B. Aubert *et al.*, *Measurement of $B^0 \rightarrow D_s^{(*)+} D^{*-}$ branching fractions and $B^0 \rightarrow D_s^{(*)+} D^{*-}$ polarization with a partial reconstruction technique*, Phys. Rev. **D67** (2003) 092003, [arXiv:hep-ex/0302015](#).
- [2] Particle Data Group, P. A. Zyla *et al.*, *Review of particle physics*, Prog. Theor. Exp. Phys. **2020** (2020) 083C01.

- [3] G. Kramer and W. F. Palmer, *Branching ratios and CP asymmetries in the decay $B \rightarrow VV$* , Phys. Rev. **D45** (1992) 193.
- [4] CLEO collaboration, S. Ahmed *et al.*, *Measurements of $B \rightarrow D_{(s)}^{(*)+} D^{(*)+}$ branching fractions*, Phys. Rev. **D62** (2000) 112003, arXiv:hep-ex/0008015.
- [5] CLEO collaboration, J. E. Duboscq and others", *Measurement of the Form Factors for $\bar{B}^0 \rightarrow D^{*+} \ell^- \bar{\nu}$* , Phys. Rev. Lett. **76** (1996) 3898.
- [6] Z. Luo and J. L. Rosner, *Factorization in color-favored b-meson decays to charm*, Phys. Rev. **D64** (2001) 094001.
- [7] M. Suzuki, *Final-state interactions and s^- quark helicity conservation in $B \rightarrow J/\psi K^*$* , Phys. Rev. **D64** (2001) 117503, arXiv:hep-ph/0106354.
- [8] LHCb collaboration, R. Aaij *et al.*, *Test of lepton flavor universality by the measurement of the $B^0 \rightarrow D^{*-} \tau^+ \nu_\tau$ branching fraction using three-prong τ decays*, Phys. Rev. **D97** (2018) 072013, arXiv:1711.02505.
- [9] D. Hill, M. John, W. Ke, and A. Poluektov, *Model-independent method for measuring the angular coefficients of $B^0 \rightarrow D^{*-} \tau^+ \nu_\tau$ decays*, JHEP **11** (2019) 133, arXiv:1908.04643.
- [10] LHCb collaboration, R. Aaij *et al.*, *Angular analysis of the $B^0 \rightarrow K^{*0} \mu^+ \mu^-$ decay using 3 fb^{-1} of integrated luminosity*, JHEP **02** (2016) 104, arXiv:1512.04442.
- [11] LHCb collaboration, R. Aaij *et al.*, *Angular analysis of the $B^+ \rightarrow K^{*+} \mu^+ \mu^-$ decay*, Phys. Rev. Lett. **126** (2021) 161802, arXiv:2012.13241.
- [12] LHCb collaboration, A. A. Alves Jr. *et al.*, *The LHCb detector at the LHC*, JINST **3** (2008) S08005.
- [13] LHCb collaboration, R. Aaij *et al.*, *LHCb detector performance*, Int. J. Mod. Phys. **A30** (2015) 1530022, arXiv:1412.6352.
- [14] T. Sjöstrand, S. Mrenna, and P. Skands, *A brief introduction to PYTHIA 8.1*, Comput. Phys. Commun. **178** (2008) 852, arXiv:0710.3820; T. Sjöstrand, S. Mrenna, and P. Skands, *PYTHIA 6.4 physics and manual*, JHEP **05** (2006) 026, arXiv:hep-ph/0603175.
- [15] I. Belyaev *et al.*, *Handling of the generation of primary events in Gauss, the LHCb simulation framework*, J. Phys. Conf. Ser. **331** (2011) 032047.
- [16] D. J. Lange, *The EvtGen particle decay simulation package*, Nucl. Instrum. Meth. **A462** (2001) 152.
- [17] N. Davidson, T. Przedzinski, and Z. Was, *PHOTOS interface in C++: Technical and physics documentation*, Comp. Phys. Comm. **199** (2016) 86, arXiv:1011.0937.
- [18] Geant4 collaboration, J. Allison *et al.*, *Geant4 developments and applications*, IEEE Trans. Nucl. Sci. **53** (2006) 270; Geant4 collaboration, S. Agostinelli *et al.*, *Geant4: A simulation toolkit*, Nucl. Instrum. Meth. **A506** (2003) 250.

- [19] M. Clemencic *et al.*, *The LHCb simulation application, Gauss: Design, evolution and experience*, J. Phys. Conf. Ser. **331** (2011) 032023.
- [20] D. Müller, M. Clemencic, G. Corti, and M. Gersabeck, *ReDecay: A novel approach to speed up the simulation at LHCb*, Eur. Phys. J. **C78** (2018) 1009, [arXiv:1810.10362](#).
- [21] G. A. Cowan, D. C. Craik, and M. D. Needham, *RapidSim: an application for the fast simulation of heavy-quark hadron decays*, Comput. Phys. Commun. **214** (2017) 239, [arXiv:1612.07489](#).
- [22] W. D. Hulsbergen, *Decay chain fitting with a Kalman filter*, Nucl. Instrum. Meth. **A552** (2005) 566, [arXiv:physics/0503191](#).
- [23] LHCb collaboration, R. Aaij *et al.*, *Precise measurement of the f_s/f_d ratio of hadronisation fractions and of B_s^0 decay branching fractions*, [arXiv:2103.06810](#), Submitted to PRD.
- [24] T. Skwarnicki, *A study of the radiative cascade transitions between the Upsilon-prime and Upsilon resonances*, PhD thesis, Institute of Nuclear Physics, Krakow, 1986, DESY-F31-86-02.
- [25] LHCb collaboration, R. Aaij *et al.*, *Measurement of CP observables in $B^\pm \rightarrow D^{(*)}K^\pm$ and $B^\pm \rightarrow D^{(*)}\pi^\pm$ decays*, Phys. Lett. **B777** (2018) 16, [arXiv:1708.06370](#).
- [26] LHCb collaboration, R. Aaij *et al.*, *Measurement of CP observables in $B^\pm \rightarrow D^{(*)}K^\pm$ and $B^\pm \rightarrow D^{(*)}\pi^\pm$ decays using two-body D final states*, JHEP **04** (2021) 081, [arXiv:2012.09903](#).
- [27] M. Pivk and F. R. Le Diberder, *sPlot: A statistical tool to unfold data distributions*, Nucl. Instrum. Meth. **A555** (2005) 356, [arXiv:physics/0402083](#).
- [28] J. Eschle, A. Puig Navarro, R. Silva Coutinho, and N. Serra, *zfit: Scalable pythonic fitting*, SoftwareX **11** (2020) 100508, [arXiv:1910.13429](#).
- [29] C. Langenbruch, *Parameter uncertainties in weighted unbinned maximum likelihood fits*, [arXiv:1911.01303](#).
- [30] LHCb collaboration, R. Aaij *et al.*, *Measurement of polarization amplitudes and CP asymmetries in $B^0 \rightarrow \phi K^*(892)^0$* , JHEP **05** (2014) 069, [arXiv:1403.2888](#).
- [31] BaBar collaboration, P. del Amo Sanchez *et al.*, *Measurements of branching fractions, polarizations, and direct CP-violation asymmetries in $B^+ \rightarrow \rho^0 K^{*+}$ and $B^+ \rightarrow f_0(980)K^{*+}$ decays*, Phys. Rev. **D83** (2011) 051101, [arXiv:1012.4044](#).
- [32] Belle collaboration, J. Zhang *et al.*, *Measurements of branching fractions and polarization in $B \rightarrow K^* \rho$ decays*, Phys. Rev. Lett. **95** (2005) 141801, [arXiv:hep-ex/0408102](#).
- [33] LHCb collaboration, R. Aaij *et al.*, *First observation of the decay $B_s^0 \rightarrow K^{*0} \bar{K}^{*0}$* , Phys. Lett. **B709** (2012) 50, [arXiv:1111.4183](#).

LHCb collaboration

R. Aaij³², C. Abellán Beteta⁵⁰, T. Ackernley⁶⁰, B. Adeva⁴⁶, M. Adinolfi⁵⁴, H. Afsharnia⁹, C.A. Aidala⁸⁶, S. Aiola²⁵, Z. Ajaltouni⁹, S. Akar⁶⁵, J. Albrecht¹⁵, F. Alessio⁴⁸, M. Alexander⁵⁹, A. Alfonso Alberio⁴⁵, Z. Aliouche⁶², G. Alkhazov³⁸, P. Alvarez Cartelle⁵⁵, S. Amato², Y. Amhis¹¹, L. An⁴⁸, L. Anderlini²², A. Andreianov³⁸, M. Andreotti²¹, F. Archilli¹⁷, A. Artamonov⁴⁴, M. Artuso⁶⁸, K. Arzymatov⁴², E. Aslanides¹⁰, M. Atzeni⁵⁰, B. Audurier¹², S. Bachmann¹⁷, M. Bachmayer⁴⁹, J.J. Back⁵⁶, P. Baladron Rodriguez⁴⁶, V. Balagura¹², W. Baldini²¹, J. Baptista Leite¹, R.J. Barlow⁶², S. Barsuk¹¹, W. Barter⁶¹, M. Bartolini²⁴, F. Baryshnikov⁸³, J.M. Basels¹⁴, G. Bassi²⁹, B. Batsukh⁶⁸, A. Battig¹⁵, A. Bay⁴⁹, M. Becker¹⁵, F. Bedeschi²⁹, I. Bediaga¹, A. Beiter⁶⁸, V. Belavin⁴², S. Belin²⁷, V. Bellee⁴⁹, K. Belous⁴⁴, I. Belov⁴⁰, I. Belyaev⁴¹, G. Bencivenni²³, E. Ben-Haim¹³, A. Berezhnoy⁴⁰, R. Bernet⁵⁰, D. Berninghoff¹⁷, H.C. Bernstein⁶⁸, C. Bertella⁴⁸, A. Bertolin²⁸, C. Betancourt⁵⁰, F. Betti⁴⁸, Ia. Bezshyiko⁵⁰, S. Bhasin⁵⁴, J. Bhom³⁵, L. Bian⁷³, M.S. Bieker¹⁵, S. Bifani⁵³, P. Billoir¹³, M. Birch⁶¹, F.C.R. Bishop⁵⁵, A. Bitadze⁶², A. Bizzeti^{22,k}, M. Bjørn⁶³, M.P. Blago⁴⁸, T. Blake⁵⁶, F. Blanc⁴⁹, S. Blusk⁶⁸, D. Bobulska⁵⁹, J.A. Boelhauve¹⁵, O. Boente Garcia⁴⁶, T. Boettcher⁶⁵, A. Boldyrev⁸², A. Bondar⁴³, N. Bondar^{38,48}, S. Borghi⁶², M. Borisyak⁴², M. Borsato¹⁷, J.T. Borsuk³⁵, S.A. Bouchiba⁴⁹, T.J.V. Bowcock⁶⁰, A. Boyer⁴⁸, C. Bozzi²¹, M.J. Bradley⁶¹, S. Braun⁶⁶, A. Brea Rodriguez⁴⁶, M. Brodski⁴⁸, J. Brodzicka³⁵, A. Brossa Gonzalo⁵⁶, D. Brundu²⁷, A. Buonauro⁵⁰, C. Burr⁴⁸, A. Bursche⁷², A. Butkevich³⁹, J.S. Butter³², J. Buytaert⁴⁸, W. Byczynski⁴⁸, S. Cadeddu²⁷, H. Cai⁷³, R. Calabrese^{21,f}, L. Calefice^{15,13}, L. Calero Diaz²³, S. Cali²³, R. Calladine⁵³, M. Calvi^{26,j}, M. Calvo Gomez⁸⁵, P. Camargo Magalhaes⁵⁴, A. Camboni^{45,85}, P. Campana²³, A.F. Campoverde Quezada⁶, S. Capelli^{26,j}, L. Capriotti^{20,d}, A. Carbone^{20,d}, G. Carboni³¹, R. Cardinale²⁴, A. Cardini²⁷, I. Carli⁴, P. Carniti^{26,j}, L. Carus¹⁴, K. Carvalho Akiba³², A. Casais Vidal⁴⁶, G. Casse⁶⁰, M. Cattaneo⁴⁸, G. Cavallero⁴⁸, S. Celani⁴⁹, J. Cerasoli¹⁰, A.J. Chadwick⁶⁰, M.G. Chapman⁵⁴, M. Charles¹³, Ph. Charpentier⁴⁸, G. Chatzikonstantinidis⁵³, C.A. Chavez Barajas⁶⁰, M. Chefdeville⁸, C. Chen³, S. Chen⁴, A. Chernov³⁵, V. Chobanova⁴⁶, S. Cholak⁴⁹, M. Chruszcz³⁵, A. Chubykin³⁸, V. Chulikov³⁸, P. Ciambone²³, M.F. Cicala⁵⁶, X. Cid Vidal⁴⁶, G. Ciezarek⁴⁸, P.E.L. Clarke⁵⁸, M. Clemencic⁴⁸, H.V. Cliff⁵⁵, J. Closier⁴⁸, J.L. Cobbedick⁶², V. Coco⁴⁸, J.A.B. Coelho¹¹, J. Cogan¹⁰, E. Cogneras⁹, L. Cojocariu³⁷, P. Collins⁴⁸, T. Colombo⁴⁸, L. Congedo^{19,c}, A. Contu²⁷, N. Cooke⁵³, G. Coombs⁵⁹, G. Corti⁴⁸, C.M. Costa Sobral⁵⁶, B. Couturier⁴⁸, D.C. Craik⁶⁴, J. Crkovač⁶⁷, M. Cruz Torres¹, R. Currie⁵⁸, C.L. Da Silva⁶⁷, E. Dall'Occo¹⁵, J. Dalseno⁴⁶, C. D'Ambrosio⁴⁸, A. Danilina⁴¹, P. d'Argent⁴⁸, A. Davis⁶², O. De Aguiar Francisco⁶², K. De Bruyn⁷⁹, S. De Capua⁶², M. De Cian⁴⁹, J.M. De Miranda¹, L. De Paula², M. De Serio^{19,c}, D. De Simone⁵⁰, P. De Simone²³, J.A. de Vries⁸⁰, C.T. Dean⁶⁷, D. Decamp⁸, L. Del Buono¹³, B. Delaney⁵⁵, H.-P. Dembinski¹⁵, A. Dendek³⁴, V. Denysenko⁵⁰, D. Derkach⁸², O. Deschamps⁹, F. Desse¹¹, F. Dettori^{27,e}, B. Dey⁷⁷, P. Di Nezza²³, S. Didenko⁸³, L. Dieste Maronas⁴⁶, H. Dijkstra⁴⁸, V. Dobishuk⁵², A.M. Donohoe¹⁸, F. Dordei²⁷, A.C. dos Reis¹, L. Douglas⁵⁹, A. Dovbnya⁵¹, A.G. Downes⁸, K. Dreimanis⁶⁰, M.W. Dudek³⁵, L. Dufour⁴⁸, V. Duk⁷⁸, P. Durante⁴⁸, J.M. Durham⁶⁷, D. Dutta⁶², A. Dziurda³⁵, A. Dzyuba³⁸, S. Easo⁵⁷, U. Egede⁶⁹, V. Egorychev⁴¹, S. Eidelman^{43,v}, S. Eisenhardt⁵⁸, S. Ek-In⁴⁹, L. Eklund^{59,w}, S. Ely⁶⁸, A. Ene³⁷, E. Epple⁶⁷, S. Escher¹⁴, J. Eschle⁵⁰, S. Esen¹³, T. Evans⁴⁸, A. Falabella²⁰, J. Fan³, Y. Fan⁶, B. Fang⁷³, S. Farry⁶⁰, D. Fazzini^{26,j}, M. Féo⁴⁸, A. Fernandez Prieto⁴⁶, J.M. Fernandez-tenllado Arribas⁴⁵, A.D. Fernez⁶⁶, F. Ferrari^{20,d}, L. Ferreira Lopes⁴⁹, F. Ferreira Rodrigues², S. Ferreres Sole³², M. Ferrillo⁵⁰, M. Ferro-Luzzi⁴⁸, S. Filippov³⁹, R.A. Fini¹⁹, M. Fiorini^{21,f}, M. Firlej³⁴, K.M. Fischer⁶³, D.S. Fitzgerald⁸⁶, C. Fitzpatrick⁶², T. Fiutowski³⁴, F. Fleuret¹², M. Fontana¹³, F. Fontanelli^{24,h}, R. Forty⁴⁸, V. Franco Lima⁶⁰, M. Franco Sevilla⁶⁶, M. Frank⁴⁸, E. Franzoso²¹, G. Frau¹⁷, C. Frei⁴⁸, D.A. Friday⁵⁹, J. Fu²⁵, Q. Fuehring¹⁵, W. Funk⁴⁸, E. Gabriel³²,

T. Gaintseva⁴², A. Gallas Torreira⁴⁶, D. Galli^{20,d}, S. Gambetta^{58,48}, Y. Gan³, M. Gandelman²,
 P. Gandini²⁵, Y. Gao⁵, M. Garau²⁷, L.M. Garcia Martin⁵⁶, P. Garcia Moreno⁴⁵,
 J. García Pardiñas^{26,j}, B. Garcia Plana⁴⁶, F.A. Garcia Rosales¹², L. Garrido⁴⁵, C. Gaspar⁴⁸,
 R.E. Geertsema³², D. Gerick¹⁷, L.L. Gerken¹⁵, E. Gersabeck⁶², M. Gersabeck⁶², T. Gershon⁵⁶,
 D. Gerstel¹⁰, Ph. Ghez⁸, V. Gibson⁵⁵, H.K. Giezma³⁶, M. Giovannetti^{23,p}, A. Gioventù⁴⁶,
 P. Gironella Gironell⁴⁵, L. Giubega³⁷, C. Giugliano^{21,f,48}, K. Gizdov⁵⁸, E.L. Gkougkousis⁴⁸,
 V.V. Gligorov¹³, C. Göbel⁷⁰, E. Golobardes⁸⁵, D. Golubkov⁴¹, A. Golutvin^{61,83}, A. Gomes^{1,a},
 S. Gomez Fernandez⁴⁵, F. Goncalves Abrantes⁶³, M. Goncerz³⁵, G. Gong³, P. Gorbounov⁴¹,
 I.V. Gorelov⁴⁰, C. Gotti²⁶, E. Govorkova⁴⁸, J.P. Grabowski¹⁷, T. Grammatico¹³,
 L.A. Granado Cardoso⁴⁸, E. Graugés⁴⁵, E. Graverini⁴⁹, G. Graziani²², A. Grecu³⁷,
 L.M. Greeven³², P. Griffith^{21,f}, L. Grillo⁶², S. Gromov⁸³, B.R. Gruberg Cazon⁶³, C. Gu³,
 M. Guarise²¹, P. A. Günther¹⁷, E. Gushchin³⁹, A. Guth¹⁴, Y. Guz⁴⁴, T. Gys⁴⁸,
 T. Hadavizadeh⁶⁹, G. Haefeli⁴⁹, C. Haen⁴⁸, J. Haimberger⁴⁸, T. Halewood-leagas⁶⁰,
 P.M. Hamilton⁶⁶, J.P. Hammerich⁶⁰, Q. Han⁷, X. Han¹⁷, T.H. Hancock⁶³,
 S. Hansmann-Menzemer¹⁷, N. Harnew⁶³, T. Harrison⁶⁰, C. Hasse⁴⁸, M. Hatch⁴⁸, J. He^{6,b},
 M. Hecker⁶¹, K. Heijhoff³², K. Heinicke¹⁵, A.M. Hennequin⁴⁸, K. Hennessy⁶⁰, L. Henry^{25,47},
 J. Heuel¹⁴, A. Hicheur², D. Hill⁴⁹, M. Hilton⁶², S.E. Hollitt¹⁵, J. Hu¹⁷, J. Hu⁷², W. Hu⁷,
 W. Huang⁶, X. Huang⁷³, W. Hulsbergen³², R.J. Hunter⁵⁶, M. Hushchyn⁸², D. Hutchcroft⁶⁰,
 D. Hynds³², P. Ibis¹⁵, M. Idzik³⁴, D. Ilin³⁸, P. Ilten⁶⁵, A. Inglese³⁸, A. Ishteev⁸³, K. Ivshin³⁸,
 R. Jacobsson⁴⁸, S. Jakobsen⁴⁸, E. Jans³², B.K. Jashal⁴⁷, A. Jawahery⁶⁶, V. Jevtic¹⁵,
 M. Jezabek³⁵, F. Jiang³, M. John⁶³, D. Johnson⁴⁸, C.R. Jones⁵⁵, T.P. Jones⁵⁶, B. Jost⁴⁸,
 N. Jurik⁴⁸, S. Kandybei⁵¹, Y. Kang³, M. Karacson⁴⁸, M. Karpov⁸², F. Keizer⁴⁸, M. Kenzie⁵⁶,
 T. Ketel³³, B. Khanji¹⁵, A. Kharisova⁸⁴, S. Kholodenko⁴⁴, T. Kirn¹⁴, V.S. Kirsebom⁴⁹,
 O. Kitouni⁶⁴, S. Klaver³², K. Klimaszewski³⁶, S. Koliiev⁵², A. Kondybayeva⁸³,
 A. Konoplyannikov⁴¹, P. Kopciewicz³⁴, R. Kopecna¹⁷, P. Koppenburg³², M. Korolev⁴⁰,
 I. Kostyuk^{32,52}, O. Kot⁵², S. Kotriakhova^{21,38}, P. Kravchenko³⁸, L. Kravchuk³⁹,
 R.D. Krawczyk⁴⁸, M. Kreps⁵⁶, F. Kress⁶¹, S. Kretzschmar¹⁴, P. Krokovny^{43,v}, W. Krupa³⁴,
 W. Krzemien³⁶, W. Kucewicz^{35,t}, M. Kucharczyk³⁵, V. Kudryavtsev^{43,v}, H.S. Kuindersma^{32,33},
 G.J. Kunde⁶⁷, T. Kvaratskheliya⁴¹, D. Lacarrere⁴⁸, G. Lafferty⁶², A. Lai²⁷, A. Lampis²⁷,
 D. Lancierini⁵⁰, J.J. Lane⁶², R. Lane⁵⁴, G. Lanfranchi²³, C. Langenbruch¹⁴, J. Langer¹⁵,
 O. Lantwin⁵⁰, T. Latham⁵⁶, F. Lazzari^{29,q}, R. Le Gac¹⁰, S.H. Lee⁸⁶, R. Lefèvre⁹, A. Leflat⁴⁰,
 S. Legotin⁸³, O. Leroy¹⁰, T. Lesiak³⁵, B. Leverington¹⁷, H. Li⁷², L. Li⁶³, P. Li¹⁷, S. Li⁷, Y. Li⁴,
 Y. Li⁴, Z. Li⁶⁸, X. Liang⁶⁸, T. Lin⁶¹, R. Lindner⁴⁸, V. Lisovskyi¹⁵, R. Litvinov²⁷, G. Liu⁷²,
 H. Liu⁶, S. Liu⁴, X. Liu³, A. Loi²⁷, J. Lomba Castro⁴⁶, I. Longstaff⁵⁹, J.H. Lopes²,
 G.H. Lovell⁵⁵, Y. Lu⁴, D. Lucchesi^{28,l}, S. Luchuk³⁹, M. Lucio Martinez³², V. Lukashenko³²,
 Y. Luo³, A. Lupato⁶², E. Luppi^{21,f}, O. Lupton⁵⁶, A. Lusiani^{29,m}, X. Lyu⁶, L. Ma⁴, R. Ma⁶,
 S. Maccolini^{20,d}, F. Machefert¹¹, F. Maciuc³⁷, V. Macko⁴⁹, P. Mackowiak¹⁵,
 S. Maddrell-Mander⁵⁴, O. Madejczyk³⁴, L.R. Madhan Mohan⁵⁴, O. Maev³⁸, A. Maevskiy⁸²,
 D. Maisuzenko³⁸, M.W. Majewski³⁴, J.J. Malczewski³⁵, S. Malde⁶³, B. Malecki⁴⁸, A. Malinin⁸¹,
 T. Maltsev^{43,v}, H. Malygina¹⁷, G. Manca^{27,e}, G. Mancinelli¹⁰, D. Manuzzi^{20,d},
 D. Marangotto^{25,i}, J. Maratas^{9,s}, J.F. Marchand⁸, U. Marconi²⁰, S. Mariani^{22,g},
 C. Marin Benito⁴⁸, M. Marinangeli⁴⁹, J. Marks¹⁷, A.M. Marshall⁵⁴, P.J. Marshall⁶⁰,
 G. Martellotti³⁰, L. Martinazzoli^{48,j}, M. Martinelli^{26,j}, D. Martinez Santos⁴⁶,
 F. Martinez Vidal⁴⁷, A. Massafferri¹, M. Materok¹⁴, R. Matev⁴⁸, A. Mathad⁵⁰, Z. Mathe⁴⁸,
 V. Matiunin⁴¹, C. Matteuzzi²⁶, K.R. Mattioli⁸⁶, A. Mauri³², E. Maurice¹², J. Mauricio⁴⁵,
 M. Mazurek⁴⁸, M. McCann⁶¹, L. Mcconnell¹⁸, T.H. Mcgrath⁶², A. McNab⁶², R. McNulty¹⁸,
 J.V. Mead⁶⁰, B. Meadows⁶⁵, C. Meaux¹⁰, G. Meier¹⁵, N. Meinert⁷⁶, D. Melnychuk³⁶,
 S. Meloni^{26,j}, M. Merk^{32,80}, A. Merli²⁵, L. Meyer Garcia², M. Mikhasenko⁴⁸, D.A. Milanese⁷⁴,
 E. Millard⁵⁶, M. Milovanovic⁴⁸, M.-N. Minard⁸, A. Minotti²¹, L. Minzoni^{21,f}, S.E. Mitchell⁵⁸,
 B. Mitreska⁶², D.S. Mitzel⁴⁸, A. Mödden¹⁵, R.A. Mohammed⁶³, R.D. Moise⁶¹, T. Mombächer¹⁵,

I.A. Monroy⁷⁴, S. Monteil⁹, M. Morandin²⁸, G. Morello²³, M.J. Morello^{29,m}, J. Moron³⁴,
 A.B. Morris⁷⁵, A.G. Morris⁵⁶, R. Mountain⁶⁸, H. Mu³, F. Muheim^{58,48}, M. Mulder⁴⁸,
 D. Müller⁴⁸, K. Müller⁵⁰, C.H. Murphy⁶³, D. Murray⁶², P. Muzzetto^{27,48}, P. Naik⁵⁴,
 T. Nakada⁴⁹, R. Nandakumar⁵⁷, T. Nanut⁴⁹, I. Nasteva², M. Needham⁵⁸, I. Neri²¹, N. Neri^{25,i},
 S. Neubert⁷⁵, N. Neufeld⁴⁸, R. Newcombe⁶¹, T.D. Nguyen⁴⁹, C. Nguyen-Mau^{49,x}, E.M. Niel¹¹,
 S. Nieswand¹⁴, N. Nikitin⁴⁰, N.S. Nolte¹⁵, C. Nunez⁸⁶, A. Oblakowska-Mucha³⁴, V. Obraztsov⁴⁴,
 D.P. O'Hanlon⁵⁴, R. Oldeman^{27,e}, M.E. Olivares⁶⁸, C.J.G. Onderwater⁷⁹, A. Ossowska³⁵,
 J.M. Otalora Goicochea², T. Ovsianikova⁴¹, P. Owen⁵⁰, A. Oyanguren⁴⁷, B. Pagare⁵⁶,
 P.R. Pais⁴⁸, T. Pajero⁶³, A. Palano¹⁹, M. Palutan²³, Y. Pan⁶², G. Panshin⁸⁴, A. Papanestis⁵⁷,
 M. Pappagallo^{19,c}, L.L. Pappalardo^{21,f}, C. Pappenheimer⁶⁵, W. Parker⁶⁶, C. Parkes⁶²,
 C.J. Parkinson⁴⁶, B. Passalacqua²¹, G. Passaleva²², A. Pastore¹⁹, M. Patel⁶¹, C. Patrignani^{20,d},
 C.J. Pawley⁸⁰, A. Pearce⁴⁸, A. Pellegrino³², M. Pepe Altarelli⁴⁸, S. Perazzini²⁰, D. Pereima⁴¹,
 P. Perret⁹, M. Petric^{59,48}, K. Petridis⁵⁴, A. Petrolini^{24,h}, A. Petrov⁸¹, S. Petrucci⁵⁸,
 M. Petruzzo²⁵, T.T.H. Pham⁶⁸, A. Philippov⁴², L. Pica^{29,n}, M. Piccini⁷⁸, B. Pietrzyk⁸,
 G. Pietrzyk⁴⁹, M. Pili⁶³, D. Pinci³⁰, F. Pisani⁴⁸, Resmi P.K¹⁰, V. Placinta³⁷, J. Plews⁵³,
 M. Plo Casasus⁴⁶, F. Polci¹³, M. Poli Lener²³, M. Poliakov⁶⁸, A. Poluektov¹⁰, N. Polukhina^{83,u},
 I. Polyakov⁶⁸, E. Polycarpo², G.J. Pomery⁵⁴, S. Ponce⁴⁸, D. Popov^{6,48}, S. Popov⁴²,
 S. Poslavskii⁴⁴, K. Prasanth³⁵, L. Promberger⁴⁸, C. Prouve⁴⁶, V. Pugatch⁵², H. Pullen⁶³,
 G. Punzi^{29,n}, W. Qian⁶, J. Qin⁶, R. Quagliani¹³, B. Quintana⁸, N.V. Raab¹⁸,
 R.I. Rabadan Trejo¹⁰, B. Rachwal³⁴, J.H. Rademacker⁵⁴, M. Rama²⁹, M. Ramos Pernas⁵⁶,
 M.S. Rangel², F. Ratnikov^{42,82}, G. Raven³³, M. Reboud⁸, F. Redi⁴⁹, F. Reiss⁶²,
 C. Remon Alepuz⁴⁷, Z. Ren³, V. Renaudin⁶³, R. Ribatti²⁹, S. Ricciardi⁵⁷, K. Rinnert⁶⁰,
 P. Robbe¹¹, G. Robertson⁵⁸, A.B. Rodrigues⁴⁹, E. Rodrigues⁶⁰, J.A. Rodriguez Lopez⁷⁴,
 A. Rollings⁶³, P. Roloff⁴⁸, V. Romanovskiy⁴⁴, M. Romero Lamas⁴⁶, A. Romero Vidal⁴⁶,
 J.D. Roth⁸⁶, M. Rotondo²³, M.S. Rudolph⁶⁸, T. Ruf⁴⁸, J. Ruiz Vidal⁴⁷, A. Ryzhikov⁸²,
 J. Ryzka³⁴, J.J. Saborido Silva⁴⁶, N. Sagidova³⁸, N. Sahoo⁵⁶, B. Saitta^{27,e}, M. Salomoni⁴⁸,
 D. Sanchez Gonzalo⁴⁵, C. Sanchez Gras³², R. Santacesaria³⁰, C. Santamarina Rios⁴⁶,
 M. Santimaria²³, E. Santovetti^{31,p}, D. Saranin⁸³, G. Sarpis⁵⁹, M. Sarpis⁷⁵, A. Sarti³⁰,
 C. Satriano^{30,o}, A. Satta³¹, M. Saur¹⁵, D. Savrina^{41,40}, H. Sazak⁹, L.G. Scantlebury Smead⁶³,
 S. Schael¹⁴, M. Schellenberg¹⁵, M. Schiller⁵⁹, H. Schindler⁴⁸, M. Schmelling¹⁶, B. Schmidt⁴⁸,
 O. Schneider⁴⁹, A. Schopper⁴⁸, M. Schubiger³², S. Schulte⁴⁹, M.H. Schune¹¹, R. Schwemmer⁴⁸,
 B. Sciascia²³, S. Sellam⁴⁶, A. Semennikov⁴¹, M. Senghi Soares³³, A. Sergi²⁴, N. Serra⁵⁰,
 L. Sestini²⁸, A. Seuthe¹⁵, P. Seyfert⁴⁸, Y. Shang⁵, D.M. Shangase⁸⁶, M. Shapkin⁴⁴,
 I. Shchemerov⁸³, L. Shchutska⁴⁹, T. Shears⁶⁰, L. Shekhtman^{43,v}, Z. Shen⁵, V. Shevchenko⁸¹,
 E.B. Shields^{26,j}, E. Shmanin⁸³, J.D. Shupperd⁶⁸, B.G. Siddi²¹, R. Silva Coutinho⁵⁰, G. Simi²⁸,
 S. Simone^{19,c}, N. Skidmore⁶², T. Skwarnicki⁶⁸, M.W. Slater⁵³, I. Slazyk^{21,f}, J.C. Smallwood⁶³,
 J.G. Smeaton⁵⁵, A. Smetkina⁴¹, E. Smith¹⁴, M. Smith⁶¹, A. Snoch³², M. Soares²⁰,
 L. Soares Lavra⁹, M.D. Sokoloff⁶⁵, F.J.P. Soler⁵⁹, A. Solovov³⁸, I. Solovyev³⁸,
 F.L. Souza De Almeida², B. Souza De Paula², B. Spaan¹⁵, E. Spadaro Norella^{25,i}, P. Spradlin⁵⁹,
 F. Stagni⁴⁸, M. Stahl⁶⁵, S. Stahl⁴⁸, P. Stefko⁴⁹, O. Steinkamp^{50,83}, O. Stenyakin⁴⁴, H. Stevens¹⁵,
 S. Stone⁶⁸, M.E. Stramaglia⁴⁹, M. Straticiu³⁷, D. Strelakina⁸³, F. Suljik⁶³, J. Sun²⁷, L. Sun⁷³,
 Y. Sun⁶⁶, P. Svihra⁶², P.N. Swallow⁵³, K. Swientek³⁴, A. Szabelski³⁶, T. Szumlak³⁴,
 M. Szymanski⁴⁸, S. Taneja⁶², F. Teubert⁴⁸, E. Thomas⁴⁸, K.A. Thomson⁶⁰, V. Tisserand⁹,
 S. T'Jampens⁸, M. Tobin⁴, L. Tomassetti^{21,f}, D. Torres Machado¹, D.Y. Tou¹³, M.T. Tran⁴⁹,
 E. Trifonova⁸³, C. Trippel⁴⁹, G. Tuci^{29,n}, A. Tully⁴⁹, N. Tuning^{32,48}, A. Ukleja³⁶,
 D.J. Unverzagt¹⁷, E. Ursov⁸³, A. Usachov³², A. Ustyuzhanin^{42,82}, U. Uwer¹⁷, A. Vagner⁸⁴,
 V. Vagnoni²⁰, A. Valassi⁴⁸, G. Valenti²⁰, N. Valls Canudas⁸⁵, M. van Beuzekom³²,
 M. Van Dijk⁴⁹, E. van Herwijnen⁸³, C.B. Van Hulse¹⁸, M. van Veghel⁷⁹, R. Vazquez Gomez⁴⁶,
 P. Vazquez Regueiro⁴⁶, C. Vázquez Sierra⁴⁸, S. Vecchi²¹, J.J. Velthuis⁵⁴, M. Veltri^{22,r},
 A. Venkateswaran⁶⁸, M. Veronesi³², M. Vesterinen⁵⁶, D. Vieira⁶⁵, M. Vieites Diaz⁴⁹,

H. Viemann⁷⁶, X. Vilasis-Cardona⁸⁵, E. Vilella Figueras⁶⁰, P. Vincent¹³, D. Vom Bruch¹⁰, A. Vorobyev³⁸, V. Vorobyev^{43,v}, N. Voropaev³⁸, R. Waldi¹⁷, J. Walsh²⁹, C. Wang¹⁷, J. Wang⁵, J. Wang⁴, J. Wang³, J. Wang⁷³, M. Wang³, R. Wang⁵⁴, Y. Wang⁷, Z. Wang⁵⁰, Z. Wang³, H.M. Wark⁶⁰, N.K. Watson⁵³, S.G. Weber¹³, D. Websdale⁶¹, C. Weisser⁶⁴, B.D.C. Westhenry⁵⁴, D.J. White⁶², M. Whitehead⁵⁴, D. Wiedner¹⁵, G. Wilkinson⁶³, M. Wilkinson⁶⁸, I. Williams⁵⁵, M. Williams⁶⁴, M.R.J. Williams⁵⁸, F.F. Wilson⁵⁷, W. Wislicki³⁶, M. Witek³⁵, L. Witola¹⁷, G. Wormser¹¹, S.A. Wotton⁵⁵, H. Wu⁶⁸, K. Wyllie⁴⁸, Z. Xiang⁶, D. Xiao⁷, Y. Xie⁷, A. Xu⁵, J. Xu⁶, L. Xu³, M. Xu⁷, Q. Xu⁶, Z. Xu⁵, Z. Xu⁶, D. Yang³, S. Yang⁶, Y. Yang⁶, Z. Yang³, Z. Yang⁶⁶, Y. Yao⁶⁸, L.E. Yeomans⁶⁰, H. Yin⁷, J. Yu⁷¹, X. Yuan⁶⁸, O. Yushchenko⁴⁴, E. Zaffaroni⁴⁹, M. Zavertyaev^{16,u}, M. Zdybal³⁵, O. Zenaiev⁴⁸, M. Zeng³, D. Zhang⁷, L. Zhang³, S. Zhang⁵, Y. Zhang⁵, Y. Zhang⁶³, A. Zhelezov¹⁷, Y. Zheng⁶, X. Zhou⁶, Y. Zhou⁶, X. Zhu³, Z. Zhu⁶, V. Zhukov^{14,40}, J.B. Zonneveld⁵⁸, Q. Zou⁴, S. Zucchelli^{20,d}, D. Zuliani²⁸, G. Zunica⁶².

¹*Centro Brasileiro de Pesquisas Físicas (CBPF), Rio de Janeiro, Brazil*

²*Universidade Federal do Rio de Janeiro (UFRJ), Rio de Janeiro, Brazil*

³*Center for High Energy Physics, Tsinghua University, Beijing, China*

⁴*Institute Of High Energy Physics (IHEP), Beijing, China*

⁵*School of Physics State Key Laboratory of Nuclear Physics and Technology, Peking University, Beijing, China*

⁶*University of Chinese Academy of Sciences, Beijing, China*

⁷*Institute of Particle Physics, Central China Normal University, Wuhan, Hubei, China*

⁸*Univ. Savoie Mont Blanc, CNRS, IN2P3-LAPP, Annecy, France*

⁹*Université Clermont Auvergne, CNRS/IN2P3, LPC, Clermont-Ferrand, France*

¹⁰*Aix Marseille Univ, CNRS/IN2P3, CPPM, Marseille, France*

¹¹*Université Paris-Saclay, CNRS/IN2P3, IJCLab, Orsay, France*

¹²*Laboratoire Leprince-Ringuet, CNRS/IN2P3, Ecole Polytechnique, Institut Polytechnique de Paris, Palaiseau, France*

¹³*LPNHE, Sorbonne Université, Paris Diderot Sorbonne Paris Cité, CNRS/IN2P3, Paris, France*

¹⁴*I. Physikalisches Institut, RWTH Aachen University, Aachen, Germany*

¹⁵*Fakultät Physik, Technische Universität Dortmund, Dortmund, Germany*

¹⁶*Max-Planck-Institut für Kernphysik (MPIK), Heidelberg, Germany*

¹⁷*Physikalisches Institut, Ruprecht-Karls-Universität Heidelberg, Heidelberg, Germany*

¹⁸*School of Physics, University College Dublin, Dublin, Ireland*

¹⁹*INFN Sezione di Bari, Bari, Italy*

²⁰*INFN Sezione di Bologna, Bologna, Italy*

²¹*INFN Sezione di Ferrara, Ferrara, Italy*

²²*INFN Sezione di Firenze, Firenze, Italy*

²³*INFN Laboratori Nazionali di Frascati, Frascati, Italy*

²⁴*INFN Sezione di Genova, Genova, Italy*

²⁵*INFN Sezione di Milano, Milano, Italy*

²⁶*INFN Sezione di Milano-Bicocca, Milano, Italy*

²⁷*INFN Sezione di Cagliari, Monserrato, Italy*

²⁸*Università degli Studi di Padova, Università e INFN, Padova, Padova, Italy*

²⁹*INFN Sezione di Pisa, Pisa, Italy*

³⁰*INFN Sezione di Roma La Sapienza, Roma, Italy*

³¹*INFN Sezione di Roma Tor Vergata, Roma, Italy*

³²*Nikhef National Institute for Subatomic Physics, Amsterdam, Netherlands*

³³*Nikhef National Institute for Subatomic Physics and VU University Amsterdam, Amsterdam, Netherlands*

³⁴*AGH - University of Science and Technology, Faculty of Physics and Applied Computer Science, Kraków, Poland*

³⁵*Henryk Niewodniczanski Institute of Nuclear Physics Polish Academy of Sciences, Kraków, Poland*

³⁶*National Center for Nuclear Research (NCBJ), Warsaw, Poland*

³⁷*Horia Hulubei National Institute of Physics and Nuclear Engineering, Bucharest-Magurele, Romania*

³⁸*Petersburg Nuclear Physics Institute NRC Kurchatov Institute (PNPI NRC KI), Gatchina, Russia*

- ³⁹*Institute for Nuclear Research of the Russian Academy of Sciences (INR RAS), Moscow, Russia*
- ⁴⁰*Institute of Nuclear Physics, Moscow State University (SINP MSU), Moscow, Russia*
- ⁴¹*Institute of Theoretical and Experimental Physics NRC Kurchatov Institute (ITEP NRC KI), Moscow, Russia*
- ⁴²*Yandex School of Data Analysis, Moscow, Russia*
- ⁴³*Budker Institute of Nuclear Physics (SB RAS), Novosibirsk, Russia*
- ⁴⁴*Institute for High Energy Physics NRC Kurchatov Institute (IHEP NRC KI), Protvino, Russia, Protvino, Russia*
- ⁴⁵*ICCUB, Universitat de Barcelona, Barcelona, Spain*
- ⁴⁶*Instituto Galego de Física de Altas Enerxías (IGFAE), Universidade de Santiago de Compostela, Santiago de Compostela, Spain*
- ⁴⁷*Instituto de Física Corpuscular, Centro Mixto Universidad de Valencia - CSIC, Valencia, Spain*
- ⁴⁸*European Organization for Nuclear Research (CERN), Geneva, Switzerland*
- ⁴⁹*Institute of Physics, Ecole Polytechnique Fédérale de Lausanne (EPFL), Lausanne, Switzerland*
- ⁵⁰*Physik-Institut, Universität Zürich, Zürich, Switzerland*
- ⁵¹*NSC Kharkiv Institute of Physics and Technology (NSC KIPT), Kharkiv, Ukraine*
- ⁵²*Institute for Nuclear Research of the National Academy of Sciences (KINR), Kyiv, Ukraine*
- ⁵³*University of Birmingham, Birmingham, United Kingdom*
- ⁵⁴*H.H. Wills Physics Laboratory, University of Bristol, Bristol, United Kingdom*
- ⁵⁵*Cavendish Laboratory, University of Cambridge, Cambridge, United Kingdom*
- ⁵⁶*Department of Physics, University of Warwick, Coventry, United Kingdom*
- ⁵⁷*STFC Rutherford Appleton Laboratory, Didcot, United Kingdom*
- ⁵⁸*School of Physics and Astronomy, University of Edinburgh, Edinburgh, United Kingdom*
- ⁵⁹*School of Physics and Astronomy, University of Glasgow, Glasgow, United Kingdom*
- ⁶⁰*Oliver Lodge Laboratory, University of Liverpool, Liverpool, United Kingdom*
- ⁶¹*Imperial College London, London, United Kingdom*
- ⁶²*Department of Physics and Astronomy, University of Manchester, Manchester, United Kingdom*
- ⁶³*Department of Physics, University of Oxford, Oxford, United Kingdom*
- ⁶⁴*Massachusetts Institute of Technology, Cambridge, MA, United States*
- ⁶⁵*University of Cincinnati, Cincinnati, OH, United States*
- ⁶⁶*University of Maryland, College Park, MD, United States*
- ⁶⁷*Los Alamos National Laboratory (LANL), Los Alamos, United States*
- ⁶⁸*Syracuse University, Syracuse, NY, United States*
- ⁶⁹*School of Physics and Astronomy, Monash University, Melbourne, Australia, associated to ⁵⁶*
- ⁷⁰*Pontifícia Universidade Católica do Rio de Janeiro (PUC-Rio), Rio de Janeiro, Brazil, associated to ²*
- ⁷¹*Physics and Micro Electronic College, Hunan University, Changsha City, China, associated to ⁷*
- ⁷²*Guangdong Provincial Key Laboratory of Nuclear Science, Institute of Quantum Matter, South China Normal University, Guangzhou, China, associated to ³*
- ⁷³*School of Physics and Technology, Wuhan University, Wuhan, China, associated to ³*
- ⁷⁴*Departamento de Física, Universidad Nacional de Colombia, Bogota, Colombia, associated to ¹³*
- ⁷⁵*Universität Bonn - Helmholtz-Institut für Strahlen und Kernphysik, Bonn, Germany, associated to ¹⁷*
- ⁷⁶*Institut für Physik, Universität Rostock, Rostock, Germany, associated to ¹⁷*
- ⁷⁷*Eotvos Lorand University, Budapest, Hungary, associated to ⁴⁸*
- ⁷⁸*INFN Sezione di Perugia, Perugia, Italy, associated to ²¹*
- ⁷⁹*Van Swinderen Institute, University of Groningen, Groningen, Netherlands, associated to ³²*
- ⁸⁰*Universiteit Maastricht, Maastricht, Netherlands, associated to ³²*
- ⁸¹*National Research Centre Kurchatov Institute, Moscow, Russia, associated to ⁴¹*
- ⁸²*National Research University Higher School of Economics, Moscow, Russia, associated to ⁴²*
- ⁸³*National University of Science and Technology "MISIS", Moscow, Russia, associated to ⁴¹*
- ⁸⁴*National Research Tomsk Polytechnic University, Tomsk, Russia, associated to ⁴¹*
- ⁸⁵*DS4DS, La Salle, Universitat Ramon Llull, Barcelona, Spain, associated to ⁴⁵*
- ⁸⁶*University of Michigan, Ann Arbor, United States, associated to ⁶⁸*

^a*Universidade Federal do Triângulo Mineiro (UFMT), Uberaba-MG, Brazil*

^b*Hangzhou Institute for Advanced Study, UCAS, Hangzhou, China*

^c*Università di Bari, Bari, Italy*

^d*Università di Bologna, Bologna, Italy*

- ^e *Università di Cagliari, Cagliari, Italy*
- ^f *Università di Ferrara, Ferrara, Italy*
- ^g *Università di Firenze, Firenze, Italy*
- ^h *Università di Genova, Genova, Italy*
- ⁱ *Università degli Studi di Milano, Milano, Italy*
- ^j *Università di Milano Bicocca, Milano, Italy*
- ^k *Università di Modena e Reggio Emilia, Modena, Italy*
- ^l *Università di Padova, Padova, Italy*
- ^m *Scuola Normale Superiore, Pisa, Italy*
- ⁿ *Università di Pisa, Pisa, Italy*
- ^o *Università della Basilicata, Potenza, Italy*
- ^p *Università di Roma Tor Vergata, Roma, Italy*
- ^q *Università di Siena, Siena, Italy*
- ^r *Università di Urbino, Urbino, Italy*
- ^s *MSU - Iligan Institute of Technology (MSU-IIT), Iligan, Philippines*
- ^t *AGH - University of Science and Technology, Faculty of Computer Science, Electronics and Telecommunications, Kraków, Poland*
- ^u *P.N. Lebedev Physical Institute, Russian Academy of Science (LPI RAS), Moscow, Russia*
- ^v *Novosibirsk State University, Novosibirsk, Russia*
- ^w *Department of Physics and Astronomy, Uppsala University, Uppsala, Sweden*
- ^x *Hanoi University of Science, Hanoi, Vietnam*